A RECONFIGURABLE WEARABLE SLOT ANTENNA DESIGN SUITABLE FOR SMART GLASSES

by

Erdem Çil

B.S., Electronics and Communication Engineering, Istanbul Technical University, 2017

Submitted to the Institute for Graduate Studies in
Science and Engineering in partial fulfillment of
the requirements for the degree of
Master of Science

Graduate Program in Electrical and Electronics Engineering

Boğaziçi University

2020

ACKNOWLEDGEMENTS

First and foremost, I would like to express my sincere gratitude to my advisor Assist. Prof. Sema Dumanlı Oktar for her endless support, patience and kindness. Besides being a great advisor, she always treated me as a friend and made me love the complicated world of electromagnetics. Without her guidance, I would not be able to take my first step so eagerly to my academic career.

I would like to give special thanks to all members of BOUNTENNA Research Laboratory for their contributions to this work and their friendship. They always thought of me as an elder brother and working with such a group was both an instructive and fun experience.

I would also like to thank my dear friends from BETA Laboratory: Barış Can Efe, Mustafa Becermiş, Ertaç Kızılca, Naci Pekçokgüler, Berk Çamlı, Hilmi Artun Oyman, Oğuz Kaan Erden, Semih Ramazanoğlu, Baran Demirer, Aybüke Çalıkoğlu and Deniz Özen. During the last years, I spent most of my time with them and I can never thank them enough for their friendship.

Last but not least, I would like to express my eternal gratitude to my parents, Aysel and Erdal, for their continuous support, love and trust throughout my entire life. I am very lucky to be their son. None of my achievements would have been possible without them.

This study is financially supported by Boğaziçi University Research Fund under project number 14543.

ABSTRACT

A RECONFIGURABLE WEARABLE SLOT ANTENNA DESIGN SUITABLE FOR SMART GLASSES

Wearable devices are widely used in medical applications, particularly on the purpose of remote monitoring and examination of people's health. These devices form wireless links with other electronic devices to collect diverse physiological parameters of users and to transfer the collected data to an external device. Challenges encountered in keeping the quality of wireless links above the desired level, such as detuning caused by the human body and the dynamic nature of the channels, can be overcome by the utilization of reconfigurable antennas in these devices. In this thesis, a pattern and polarization reconfigurable wearable slot antenna design operating in the 2.4 GHz Industrial, Scientific and Medical band is proposed. Glass is used as the substrate of the antenna making it suitable for smart glasses. The slot is an equilateral L-shaped slot that is fed by a coplanar waveguide feed. The reconfiguration is achieved by manipulating the slot by means of switches. Two states of switches generate two modes of operation which correspond to two L-shaped slots that are oriented in different directions and hence create patterns that are polarized in perpendicular to each other. Initially, the switching between the modes is achieved by using artificial switches. Next, a PIN diode circuitry is developed as the switching mechanism. The antenna is designed analytically, optimized through numerical analysis and fabricated. The detuning effects caused by the proximity of the human body are analysed using numerical and physical phantoms as well as human subjects. The simulation and measurement results in air, on phantoms and human subjects are compared and interpreted. Finally, a conclusion is given and possible future works are discussed.

ÖZET

AKILLI GÖZLÜK UYGULAMASINA YÖNELİK YENİDEN YAPILANDIRILABİLİR GİYİLEBİLİR YARIK ANTEN TASARIMI

Giyilebilir cihazlar, özellikle insanların sağlığının uzaktan izlenmesi ve incelenmesi amacıyla tıbbi uygulamalarda yaygın olarak kullanılmaktadır. Bu cihazlar, kullanıcıların çeşitli fizyolojik parametrelerini toplamak ve toplanan verileri harici bir cihaza aktarmak için diğer elektronik cihazlarla kablosuz bağlantı kurarlar. Kablosuz bağlantıların kalitesini istenen seviyenin üzerinde tutmada karşılaşılan, insan vücudunun neden olduğu bozulmalar ve kanalların dinamik doğası gibi zorluklar, bu cihazlarda yeniden yapılandırılabilir antenlerin kullanılmasıyla aşılabilir. Bu tezde, 2.4 GHz Sınai, Bilimsel ve Tıbbi Cihaz bandında çalışan, ışıma örüntüsü ve polarizasyonu yeniden yapılandırılabilir giyilebilir bir yarık anten tasarımı önerilmiştir. Antenin alttaşı olarak cam kullanılmıştır ve bu sayede anten akıllı gözlüklerde kullanım için uygundur. Yarık, eş düzlemli bir dalga kılavuzu ile beslenen eşkenar L-şeklinde bir yarıktır. Yeniden yapılandırma, yarığın anahtarlar yardımıyla manipüle edilmesiyle sağlanmıştır. Anahtarların iki durumu, farklı yönlere yönlendirilmiş ve böylece birbirine dik olarak polarize edilmiş desenler oluşturan iki L-şekilli yarığa karşılık gelen iki çalışma modu oluşturmaktadır. Başlangıçta, modlar arasında geçiş yapay anahtarlar kullanılarak gerçekleştirilmiştir. Daha sonra, anahtarlama mekanizması olarak bir PIN diyot devresi geliştirilmiştir. Anten analitik olarak tasarlanmış, sayısal analiz ile optimize edilmiş ve üretilmiştir. İnsan bedeninin yakınlığının yarattığı bozulma etkileri, sayısal ve fiziksel fantomların yanı sıra insan denekler kullanılarak analiz edilmiştir. Havadaki, fantomlar ve insan denekler üzerindeki simülasyon ve ölçüm sonuçları karşılaştırılmış ve yorumlanmıştır. Son olarak bir sonuç verilmiş ve gelecekteki olası çalışmalar tartışılmıştır.

TABLE OF CONTENTS

ACKNOWLEDGEMENTS i
ABSTRACT ii
ÖZET iii
LIST OF FIGURES vi
LIST OF TABLES xi
LIST OF SYMBOLS xiii
LIST OF ACRONYMS/ABBREVIATIONS xiv
1. INTRODUCTION 1
1.1. Motivation 1
1.2. Objective and Contributions of the Thesis 3
1.3. Organization of the Thesis 3
2. BACKGROUND 5
2.1. Fundamentals of Slot Antennas 5
2.1.1. Basic Concepts 5
2.1.2. Slot Antenna as the Dual of a Dipole Antenna 8
2.1.3. Dielectric Loading of Slot Antennas 10
2.2. Major Challenges in Wearable Antenna Design 11
2.3. Reconfigurable Antennas and Related Literature 13
2.3.1. Frequency Reconfiguration 15
2.3.2. Polarization Reconfiguration 15
2.3.3. Pattern Reconfiguration 16
2.4. Novelty of the Proposed Design and a Comparison with Existing Designs 17
3. PRELIMINARY MODELS 19
3.1. First Model 19
3.1.1. The Antenna Model 19
3.1.2. Analytical Design 20
3.1.3. Numerical Optimization 23
3.1.4. Results and Discussion 26

3.2. Second Model 28
3.2.1. The Antenna Model 28
3.2.2. Analytical Design 31
3.2.3. Numerical Optimization and Prototyping 34
3.2.4. Results and Discussion 37
4. OPTIMIZED MODEL 41
4.1. The Antenna Model 41
4.2. Analytical Design 42
4.3. Numerical Optimization and Prototyping 44
4.4. Results and Discussion 45
5. PIN DIODE IMPLEMENTATION 50
5.1. PIN Diode Switching Circuitry 50
5.2. Results and Discussion 52
6. ON-BODY PERFORMANCE 54
6.1. What is a Phantom? 55
6.2. Fabrication of Tissue-mimicking Mixtures 55
6.3. Measurement of Electrical Properties 57
6.3.1. Theory of the Method 57
6.3.2. Experimental Studies and Measurements 62
6.4. Completed Measurement Set-ups 63
6.5. On-body Results and Discussion 64
7. CONCLUSION 72
REFERENCES 74

LIST OF FIGURES

Figure 1.1. Some of the recent healthcare trends. 1

Figure 1.2. Data transmission via smart glasses with the wearable antenna and the general view of the smart glasses. 4

Figure 2.1. A slot on a conductive sheet. 6

Figure 2.2. (a) Parallel connected stubs (b) a simple slot. 6

Figure 2.3. The voltage and current distribution on a $\lambda/2$ long slot (Blue: Voltage, Red: Current). 7

Figure 2.4. A $\lambda/2$ long slot and its complementary dipole. 9

Figure 2.5. An offset fed $\lambda/2$ long slot matched to 50 Ω. 9

Figure 2.6. A slot antenna loaded with a dielectric material. 11

Figure 2.7. Change of the communication channel due to the mobility of humans (a) on-body communication (b) off-body communication. . . 13

Figure 2.8. Different reconfiguration techniques. 14

Figure 2.9. A comparison between the proposed antenna and related reconfigurable antennas in the literature. 18

Figure 3.1. The microstrip fed slot antenna model. 20

Figure 3.2. The parameters to be determined to optimize the performance of the microstrip fed antenna. 21

Figure 3.3. The equivalent circuit of a single microstrip fed slot antenna. . . . 24

Figure 3.4. The equivalent circuit of the first model for two modes of operation (a) the horizontal mode (b) the vertical mode. 25

Figure 3.5. Simulated frequency responses of the first model in air. 27

Figure 3.6. The standard bidirectional radiation pattern of a horizontally aligned slot antenna (left) and the simulated radiation pattern of the horizontal mode (right) (unit: dBi) (a) 3D patterns (b) 2D patterns at $\phi = 0^\circ$ (c) 2D patterns at $\theta = 90^\circ$. 29

Figure 3.7. The standard bidirectional radiation pattern of a vertically aligned slot antenna (left) and the simulated radiation pattern of the vertical mode (right) (unit: dBi) (a) 3D patterns (b) 2D patterns at $\phi = 0^\circ$ (c) 2D patterns at $\theta = 90^\circ$. 30

Figure 3.8. The electric field distribution on the antenna and the feed line for the horizontal (left) and vertical (right) mode. 31

Figure 3.9. The cavity backed slot antenna model. 32

Figure 3.10. The parameters to be determined to optimize the performance of the CBS antenna. 33

Figure 3.11. The equivalent circuit of the second model for two modes of operation (a) the horizontal mode (b) the vertical mode. 35

Figure 3.12. The prototype of the CBS antenna. 36

Figure 3.13. Simulated frequency responses of the second model in air. 37

Figure 3.14. Simulated 3D and 2D radiation patterns (Blue: $\phi = 0°$, Orange: $\phi = 90°$) of the second model (unit: dBi) (a) the horizontal mode (b) the vertical mode. 38

Figure 3.15. Measured frequency responses of the second model in air for three distinct prototypes. 40

Figure 4.1. The optimized CPW fed slot antenna model. 42

Figure 4.2. The parameters to be determined to optimize the performance of the CPW fed antenna. 43

Figure 4.3. The prototype of the optimized model. 45

Figure 4.4. Simulated and measured frequency responses of the optimized model in air. 46

Figure 4.5. Simulated 3D and 2D radiation patterns (Blue: $\phi = 0°$, Orange: $\phi = 90°$) of the optimized model in air (unit: dBi) (a) the horizontal mode (b) the vertical mode. 48

Figure 4.6. Measured normalized 3D and 2D radiation patterns (Blue: $\phi = 0°$, Orange: $\phi = 90°$) of the optimized model in air for the horizontal mode. 49

Figure 5.1. The optimized CPW fed slot antenna model with PIN diodes. . . 51

Figure 5.2. The prototype of the optimized model with PIN diodes inserted into a 3D glasses frame. 52

Figure 5.3. Measured frequency responses of the optimized model with PIN diodes in air. 53

Figure 6.1. The procedure to be followed to develop the tissue-mimicking mixtures. 58

Figure 6.2. The open-ended coaxial probe model. 59

Figure 6.3. Measurements taken in the reference mediums (a) air (b) deionized water. 62

Figure 6.4. The computed dielectric loss factor and relative permittivity of ethanol. 63

Figure 6.5. The steps to prepare the two-layer phantom. 65

Figure 6.6. Set-ups used to evaluate the on-body performance of the antenna and their numerical counterparts (a) numeric two-layer phantom (b) physical two-layer phantom (c) the antenna worn by a human (d) ANSYS human body phantom. 66

Figure 6.7. Simulated and measured frequency responses of the optimized model on the two-layer phantom and on ANSYS human body phantom. . 67

Figure 6.8. Measured frequency responses of the optimized model with both the artificial switches and PIN diodes on human subjects. 69

Figure 6.9. Simulated 3D and 2D radiation patterns (Blue: $\phi = 0°$, Orange: $\phi = 90°$) of the optimized model on ANSYS human body phantom (unit: dBi) (a) the horizontal mode (b) the vertical mode. 70

Figure 6.10. Simulated SAR of the optimized model for two modes of operation (unit: W/kg) (a) the horizontal mode (b) the vertical mode. . . . 71

LIST OF TABLES

Table 3.1. The calculated and optimized values of the parametrized dimensions for the first model. 26

Table 3.2. The center frequency and the magnitude of the reflection coefficient for the first model in air. 27

Table 3.3. The calculated and optimized values of the parametrized dimensions for the second model. 36

Table 3.4. The center frequency and the magnitude of the reflection coefficient for the second model in air. 38

Table 3.5. The value and the position of the maximum gain and the null for the second model. 39

Table 3.6. The measured center frequency and the magnitude of the reflection coefficient for three distinct prototypes of the second model. 40

Table 4.1. The calculated and optimized values of the parametrized dimensions for the optimized model. 45

Table 4.2. The center frequency, the magnitude of the reflection coefficient and the bandwidth for the optimized model in air. 47

Table 4.3. The value and the position of the maximum gain and the null for the optimized model. 49

Table 5.1. The center frequency and the magnitude of the reflection coefficient for the optimized model with PIN diodes in air. 53

Table 6.1. Electrical properties of the eye tissue and the muscle tissue at 2.45 GHz. 56

Table 6.2. The quantity of each ingredient required per 100 g mixture. 56

Table 6.3. Computed electrical properties of the two tissue-mimicking mixtures and the real values at 2.45 GHz. 64

Table 6.4. The center frequency and the magnitude of the reflection coefficient for the optimized model on the two-layer phantom and on ANSYS human body phantom. 68

Table 6.5. The mean and the standard deviation of the center frequency and the magnitude of the reflection coefficient measured on human subjects. 69

LIST OF SYMBOLS

c	Speed of light in free space
C	Capacitance
f	Frequency in Hertz
ff	Filling factor
L	Inductance
Y	Admittance
Z	Impedance
β	Propagation constant
Γ	Reflection coefficient
ϵ	Permittivity
ϵ_0	Permittivity of free space
ϵ_{eff}	Effective permittivity
ϵ_r	Relative permittivity
$\epsilon_r^{''}$	Dielectric loss factor
η_0	Intrinsic impedance of free space
λ	Wavelength
λ_0	Free space wavelength
λ_g	Guided wavelength
μ	Permeability
μ_0	Permeability of free space
ρ_e	Envelope correlation
σ	Conductivity
ω	Radial frequency in radians per second

LIST OF ACRONYMS/ABBREVIATIONS

2D	2-Dimensional
3D	3-Dimensional
BAN	Body Area Network
CBS	Cavity Backed Slot
CPW	Coplanar Waveguide
DC	Direct Current
HFSS	High Frequency Structure Simulator
IoHT	Internet of Health Things
IoT	Internet of Things
ISM	Industrial, Scientific and Medical
LCP	Liquid Crystal Polymer
MEMS	Microelectromechanical Systems
PET	Polyethylene Terephthalate
PLA	Polylactic Acid
RF	Radio Frequency
SAR	Specific Absorption Rate
TEM	Transverse Electromagnetic
VNA	Vector Network Analyzer

1. INTRODUCTION

1.1. Motivation

In recent years, the Internet of Things (IoT) has acquired high attention and been considered as a research area of innovation and growth. The IoT is a concept that makes use of a variety of objects that are able to communicate with each other and cooperate with other objects via wireless and wired connections in order to accomplish common objectives or generate new applications. The main purpose of the IoT is to create a connected set of anyone and anything to enable advanced services [1]. The IoT is benefited from in a wide range of fields such as energy, industry and healthcare. Among these different fields, the Internet of Things in healthcare, or simply the Internet of Health Things (IoHT), is accepted as one of the most appealing and promising application areas of the IoT [2]. Some of the recent healthcare trends enabled by the use of the IoHT is illustrated in Figure 1.1 [3].

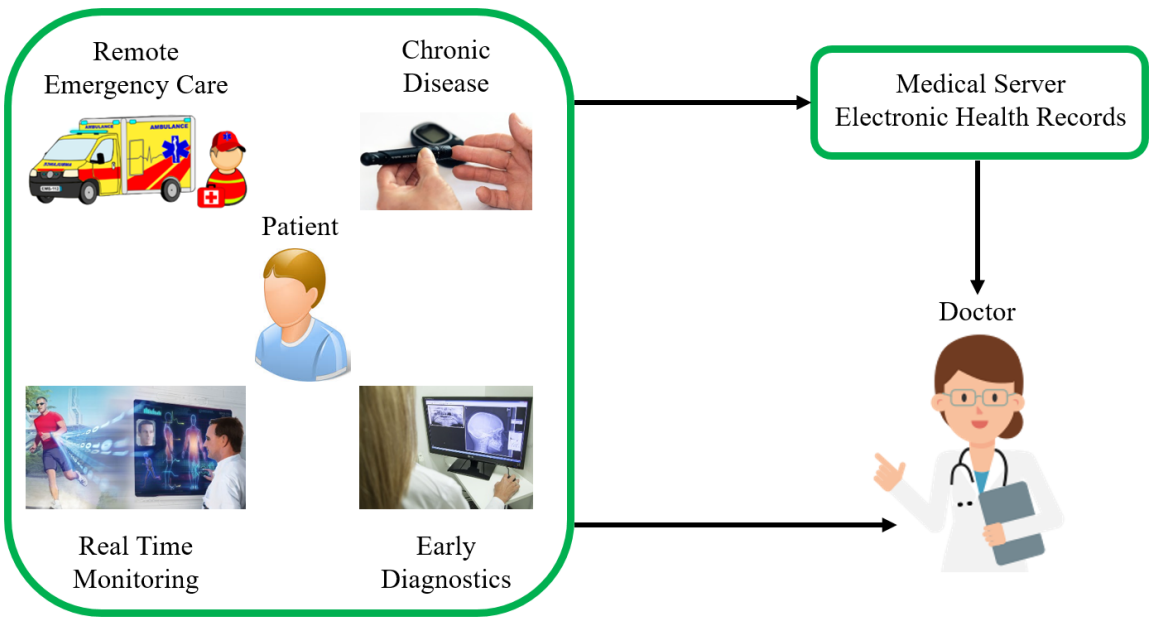

Figure 1.1. Some of the recent healthcare trends.

Due to the improvements in the field of medicine, the average duration of life of humans has been extended. While it appears to be a positive thing, ageing of the population has also brought along some problems. Considering the fact that people who need continuous medical care are mostly old people, it can be estimated that due to this ageing, the current medical system will not be sufficient in the near future and require some urgent improvements. To lessen this burden on the medical system, the IoHT focuses on remote monitoring and examination of people's current health condition. Advances in electronic technology have enabled the development of small and smart electronic devices that can be placed on or inside the human body [4]. These wearable and implantable devices form the basis of the IoHT, as they are able to continuously monitor diverse physiological parameters such as blood pressure and heart rate of healthy individuals or patients. The remote monitoring helps reduce medical costs and improve people's quality of life as well as provides timely assistance and instant care of medical staff in risky situations [5]. Owing to their benefits to the medical system, there has been a serious growth in the use of wearable devices in medical applications in the past few years and it is predicted to continue growing in the near future [6].

Wearable devices require various components to operate efficiently, thus their design is highly multidisciplinary. However, it can be argued that the antenna is one of the most important elements in a wearable device as it can significantly contribute to the overall efficiency of a wireless link [7]. A wearable antenna must be designed such that the requirements of the communication link that can vary depending on the altering environmental conditions are satisfied in order for a link to be formed efficiently. In addition, wearable antennas need to be unobtrusive and should be able to operate with minimum degradation near the hostile human body. In brief, careful design of the wearable antenna is a crucial aspect to provide a wireless communication link with the optimum solution.

1.2. Objective and Contributions of the Thesis

The objective of this thesis is to develop a pattern and polarization reconfigurable wearable antenna that is suitable for the use in smart glasses. The antenna to be designed must be able to transmit the data to an off-body device as shown in Figure 1.2. A switching mechanism must be realized on the antenna in order to reconfigure the radiation pattern. As it is a wearable antenna, it must be verified that the antenna operates efficiently not only in air but also near the human body.

For this purpose, a novel pattern and polarization reconfigurable slot antenna operating in the 2.4 GHz Industrial, Scientific and Medical (ISM) band is designed. The slot antenna is preferred for the design since due to their magnetic nature, slot antennas are more robust against detuning effects than many other types of antennas. The antenna is fed by a single coplanar waveguide (CPW) feed. To make it suitable for smart glasses, glass is utilized as the substrate of the antenna. Four PIN diodes that are biased externally are used to realize the switching mechanism required to reconfigure the radiation pattern. The slot is manipulated via these switches to create two modes of operation with different polarizations and patterns. Measurement set-ups consisting of phantoms and human subjects are developed in order to evaluate the on-body performance of the antenna. In the light of the results in air and on the measurement set-ups, the prosed antenna is determined to be promising for the intended application.

1.3. Organization of the Thesis

Throughout the thesis; the antenna model is developed, the switching mechanism is implemented using PIN diodes, set-ups are prepared for on-body measurements of the antenna and the simulation and measurement results in air, on phantoms as well as on real human bodies are given and interpreted. The thesis is organized as follows. In Chapter 1, wearable networks are introduced and the objective and the contributions of the thesis are explained. In Chapter 2, detailed background on slot

antennas, wearable antenna design challenges and reconfigurable antennas is provided. The literature for reconfigurable antennas is given and the novelty of the design along with a comparison with the related literature is explained in Chapter 2 as well. In Chapter 3, two preliminary antenna models are given along with their results in air and the reasons for the need for a more developed model are discussed. Chapter 4 presents the optimized final antenna model with a CPW feed as well as its results in air. Chapter 5 presents the implementation of PIN diodes as the switching mechanism on the optimized model. In Chapter 6, the formation of the set-ups used to evaluate the on-body performance of the antenna is explained and the on-body results are given. Finally, Chapter 7 concludes the work and discusses possible future works.

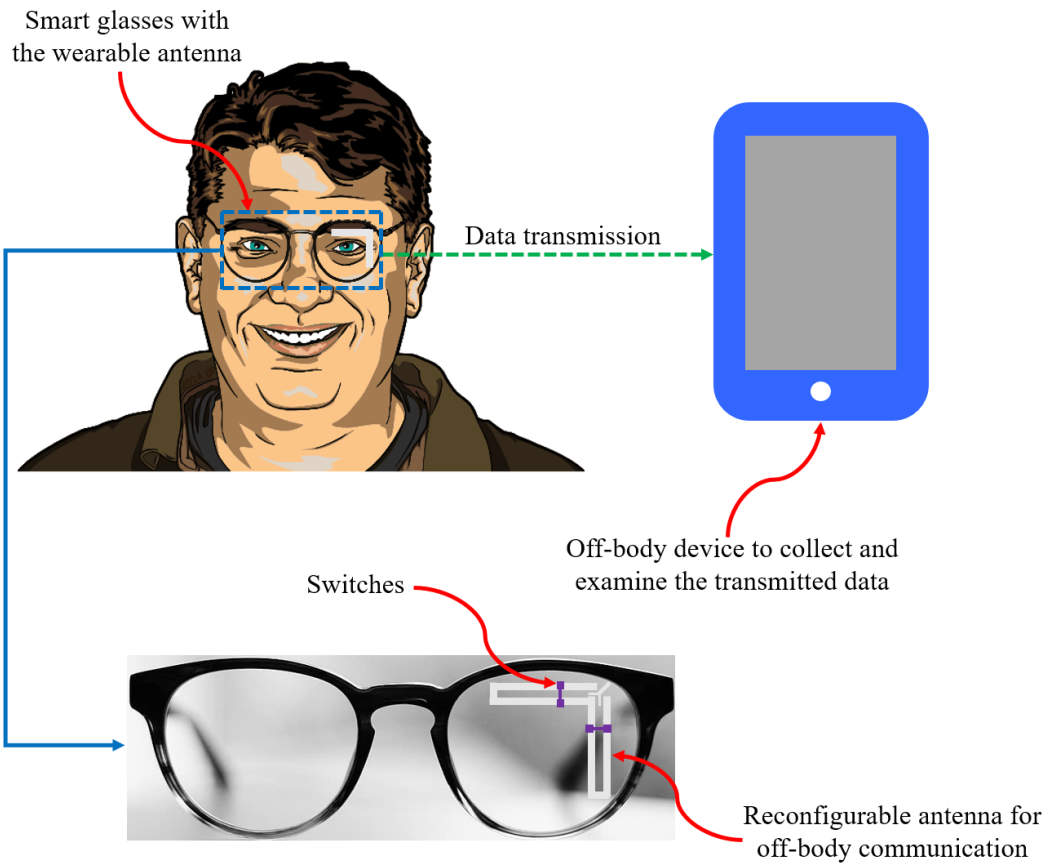

Figure 1.2. Data transmission via smart glasses with the wearable antenna and the general view of the smart glasses.

2. BACKGROUND

This chapter provides the background required to understand the basics of slot antennas, major wearable antenna design challenges as well as the reconfigurability of antennas. In Section 2.1, fundamental concepts related to slot antennas are presented. In Section 2.2, major challenges encountered in wearable antenna design are explained. Section 2.3 presents reconfigurable antennas and types of reconfiguration along with the related literature. Finally, the novelty of the proposed design and a comparison between the proposed design and related reconfigurable antennas in the literature are given in Section 2.4.

2.1. Fundamentals of Slot Antennas

2.1.1. Basic Concepts

A slot antenna is a special type of aperture antennas that is formed by cutting an opening on a conductive sheet as visualized in Figure 2.1. The conductive sheet is called the ground plane of the antenna. The opening is referred to as a slot rather than an aperture; since in general, the length (L) of the opening is much longer than its width (W). In other words, a slot is a narrow-width opening on a ground plane. Typically, the length of a slot is around half a wavelength ($\lambda/2$), whereas its width is around 0.02 of a wavelength ($\lambda/50$). This narrow slot assumption forms the basis of the approximations for slot antennas [8].

A $\lambda/2$ long slot on a conductive sheet resembles two stubs each of which consists of a two-wire transmission line that is terminated in short-circuit as visualized in Figure 2.2. The configuration shown in Figure 2.2(a) is an inefficient radiator since the long wires are placed in close proximity to each other ($W << \lambda$) and carry currents in opposite phase so that the fields created by them cancel each other. Although the end wires carry currents in the same phase, they are not long enough to radiate efficiently.

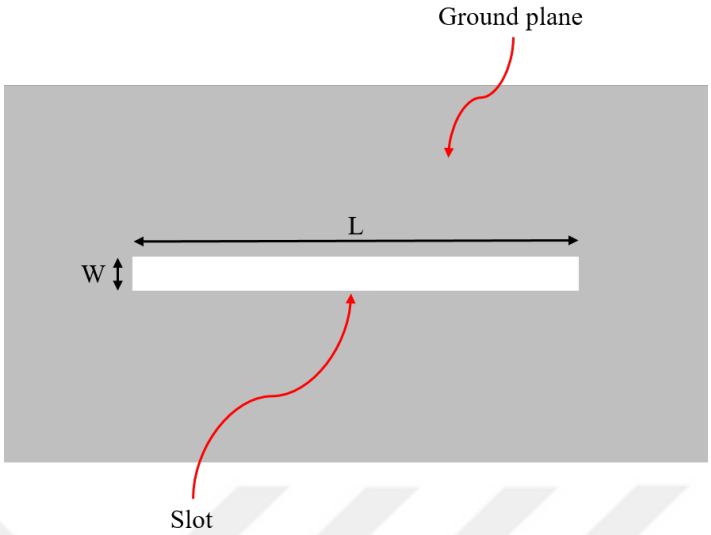

Figure 2.1. A slot on a conductive sheet.

However, the simple slot shown in Figure 2.2(b) is a very efficient radiator. When it is excited by a voltage source across its width, electric field is created across its length. The electric current flow is not limited to the edges of the slot but the currents spread out over the ground plane. The electromagnetic energy is radiated through the slot into the surrounding medium or vice-versa [9].

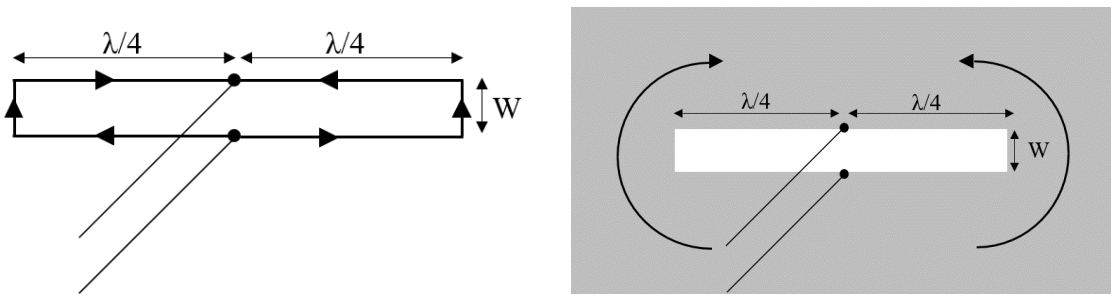

(a) (b)

Figure 2.2. (a) Parallel connected stubs (b) a simple slot.

The voltage excited across the slot propagates along the slotline toward its short-circuited ends and is reflected from these terminations. As a result of the combination of

two waves propagating in opposite directions, a standing wave is created on the slot [10]. The voltage and current distribution on a $\lambda/2$ long slot are shown in Figure 2.3. As can be seen, the voltage and the current are 90° out of phase. The voltage-maximum occurs at the center, whereas the voltage-minimums occur at the short-circuited ends. The voltage is zero at the ends due to the fact that the voltage reflection coefficient for a short-circuit termination equals to -1. In other words, the incident and reflected waves are 180° out of phase and therefore cancel each other at the ends of the slot. Contrary to the voltage distribution, the current is negative at one end, reaches its zero at the center and is positive at the other end or vice-versa in polarity. The center of the slot, where the voltage is at its maximum and the current is zero, has theoretically infinite practically very large impedance [8]. This impedance will be analysed analytically in the next subsection.

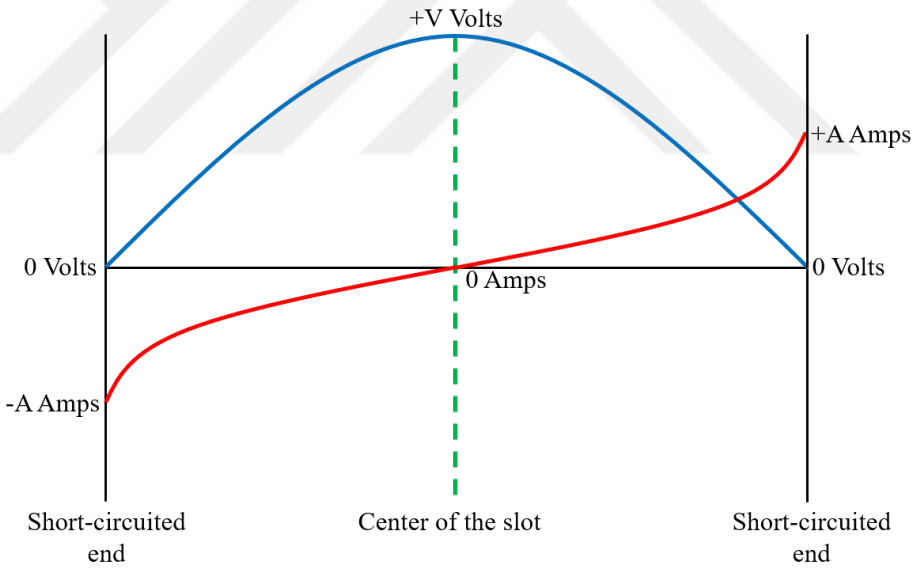

Figure 2.3. The voltage and current distribution on a $\lambda/2$ long slot (Blue: Voltage, Red: Current).

2.1.2. Slot Antenna as the Dual of a Dipole Antenna

Frequently, an antenna problem arises for the antennas that are dual of an antenna for which the solution to the same problem is already known. If two antennas are dual of each other, the fields of one of the antennas can be determined from the fields of the other one using the principle of duality [11]. In addition, the input impedances of dual antennas (Z_S and Z_C) are related to each other by Babinet's principle that is expressed as

$$Z_S Z_C = \frac{\eta_0^2}{4} \tag{2.1}$$

where η_0 is the intrinsic impedance of free space that is calculated to be 376.7 Ω by

$$\eta_0 = \sqrt{\frac{\mu_0}{\epsilon_0}} \tag{2.2}$$

The principle of duality can be applied to slot antennas as well. A $\lambda/2$ long, narrow slot can be considered as the dual of a half-wave dipole as shown in Figure 2.4, where the $\lambda/4$ long arms of the dipole in air are replaced by the slot on the conductive sheet. As the slot is the dual of a dipole, its input resistance (R_{slot}) can be related to that of a dipole (R_{dipole}) by

$$R_{slot} = \frac{\eta_0^2}{4R_{dipole}} \tag{2.3}$$

which is a consequence of the Babinet's principle given in Equation 2.1. Given that the ideal thin-wire input resistance of the complementary dipole is 73 Ω, the input resistance of a center-fed slot can be calculated to be 487 Ω. As the characteristic impedance of a transmission line is generally much less than 487 Ω, a center-fed slot is poorly matched. However, considering the voltage and current distribution given in Figure 2.3, it can be observed that moving the feed point from the center to one of the short-circuited ends results in a decrease in the ratio between the voltage and the current as well as the input resistance. Therefore, an off-center feed can be utilized to

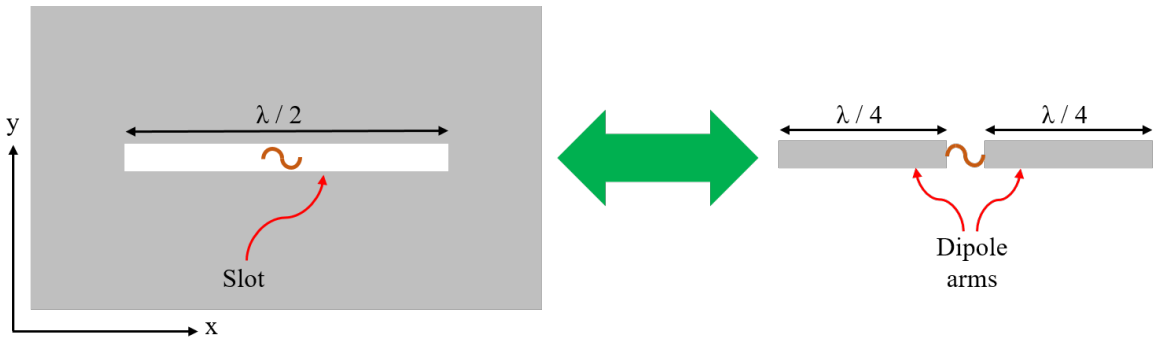

Figure 2.4. A $\lambda/2$ long slot and its complementary dipole.

achieve a better impedance match for a slot antenna. For a typical 50 Ω transmission line, the feeding must be around $\lambda/5$ away from the center of the slot as shown in Figure 2.5 [9].

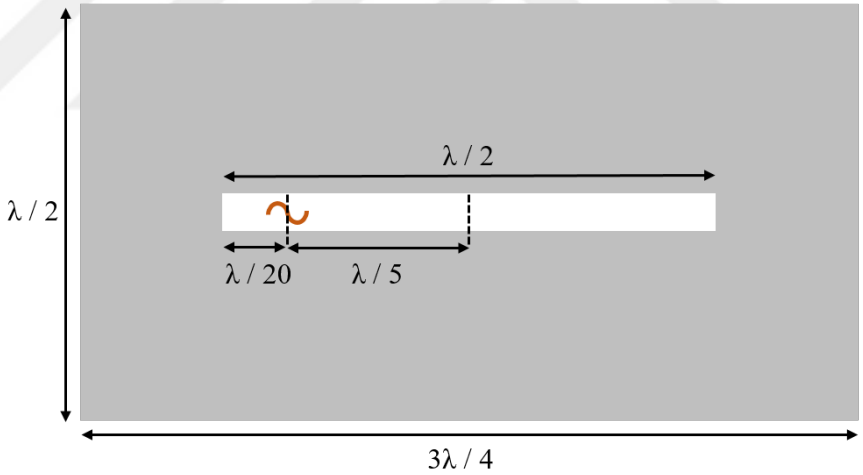

Figure 2.5. An offset fed $\lambda/2$ long slot matched to 50 Ω.

A slot antenna radiates both in the forward and backward directions of the ground plane. In other words, the radiation from a slot antenna is bidirectional. The distribution of the electric currents on the ground plane is difficult to determine; thus, they are replaced by equivalent simpler magnetic currents. The radiated fields from the slot antenna are determined by using the distribution of these fictitious magnetic cur-

rents [10]. The shape of the radiation pattern of a slot antenna is identical to that of a dipole antenna except that the E-fields and H-fields are interchanged. The polarization of the waves is dependent on the orientation of the slot. The slot antenna visualized in Figure 2.4 is polarized in y-direction; whereas the dipole antenna given in the same figure is polarized in x-direction. The radiation from the slot is at its strongest in the direction normal to the surface of the ground plane [8].

2.1.3. Dielectric Loading of Slot Antennas

When one surface of the ground plane is covered with a dielectric material other than air as shown in Figure 2.6, the slot antenna is said to be a dielectric-loaded slot antenna. The dielectric material is referred to as the substrate of the antenna. The electric field created by a dielectric-loaded slot antenna is contained not only in air but also in the dielectric material. Hence, the length of the slot is no longer equal to the half of the free space wavelength and is calculated using

$$L = \frac{\lambda_g}{2} \tag{2.4}$$

where λ_g is the guided wavelength that is given as

$$\lambda_g = \frac{\lambda_0}{\sqrt{\epsilon_{eff}}} \tag{2.5}$$

It is necessary to use an effective permittivity, ϵ_{eff}, to calculate the guided wavelength, as the waves are contained in two different dielectric media as mentioned before [12]. The effective permittivity can be considered as the relative permittivity of an equivalent medium covering all sides of the antenna that represents both air and the dielectric material. It can be calculated by

$$\epsilon_{eff} = \epsilon_r * ff + (1 - ff) \tag{2.6}$$

where the filling factor, ff, is a measure of the percentage of the electric fields cutting through the substrate. Note that when the slot is loaded with a dielectric material, other parameters mentioned in Subsection 2.1.2 must be given in terms of the guided wavelength as well.

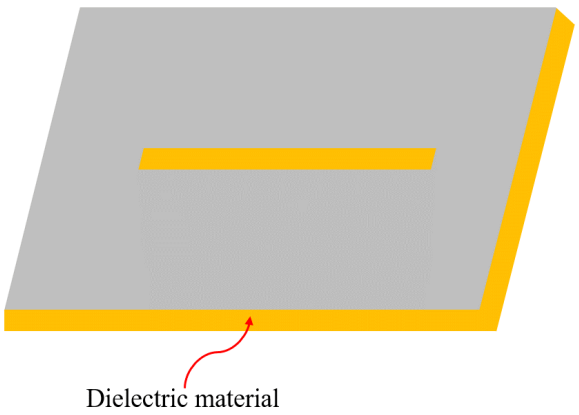

Figure 2.6. A slot antenna loaded with a dielectric material.

2.2. Major Challenges in Wearable Antenna Design

Wearable antenna design has its unique challenges that must be taken into consideration during the design process. These challenges must be tackled in order to achieve the desired performance with stability in a wireless communication system [13]. Although the severity of different challenges may depend on the intended application, most of the challenges exist in the context of the wearable implementation [7].

Firstly, along with the battery, the antenna is one of the largest components of a wearable device. However, a wearable antenna is required to be small or flexible so that it does not restrict any user activity while it is worn by the user [14]. The restrictions in size for the convenience of the users make the design of a wearable antenna difficult, since several design parameters determining the performance of the antenna, such as gain, efficiency and bandwidth, are directly related to the physical size [4].

Secondly, when a wearable antenna is placed near the human body, the body exists in the near-field of the antenna and the interaction between them becomes inevitable. Human tissues are inhomogeneous formations that have high relative permittivities as they contain large amounts of water. In addition, most of them have notable conductivities [15]. Due to the high electrical properties of human tissues, the human body presents a medium that is intrinsically lossy and hostile to the efficient electromagnetic radiation [16]. The interaction between the two results in a degradation of antenna efficiency due to bulk power absorption, detuning effects such as a shift in resonant frequency, changes in the input impedance of the antenna as well as radiation pattern distortion [17]. The effect of the human body differs from person to person due to the varying body composition of particular individuals. Moreover, it depends on the part of the body near which the antenna is located. The negative effects caused by the body may lead to a decrease in the quality of the wireless link or even loss of the link in extreme cases [18]. Hence, a wearable antenna must be designed such that minimum degradation and detuning occur when operating in proximity to the human body [7]. Preferably, a body phantom may be included in the design process in order to evaluate the on-body performance of a wearable antenna [14]. Phantoms are described in detail in Section 6.1.

Lastly, depending on the intended application, a wearable antenna may require to form more than one type of communication links, e.g. both on-body and off-body. In such a case, the wearable antenna must be able to form a high quality link for all intended types of links [14]. Furthermore, due to the mobility of humans, the communication channel is inherently dynamic. In other words, the communication channel is constantly changing for both on-body and off-body communication as visualized in Figure 2.7. In such dynamic cases, altering environmental conditions lead to significant channel fading even during normal activity, since the current position of the user significantly affects the quality of the link and the energy efficiency of the antenna, which is an important factor in terms of battery lifetime. As it is not possible to separate the performance of a wearable antenna from the characteristics of the channels, changing channels must be taken into account during the design process [19]. In brief, as the

user moves around, a wearable antenna must be able to operate efficiently while the link quality is maintained above the desired level [20].

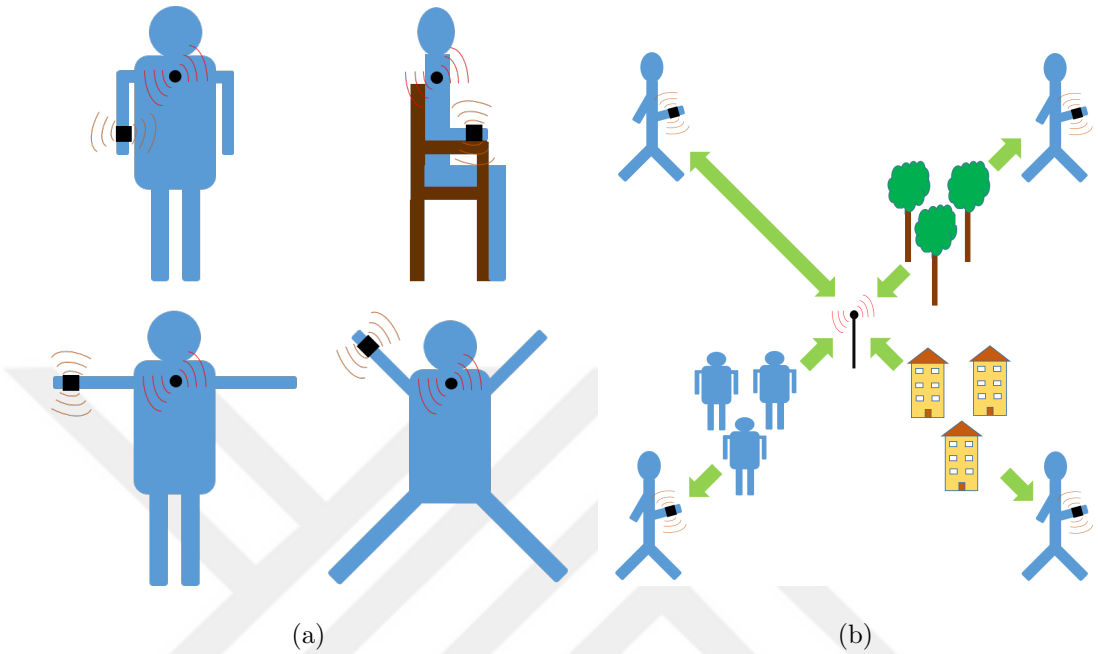

Figure 2.7. Change of the communication channel due to the mobility of humans (a) on-body communication (b) off-body communication.

2.3. Reconfigurable Antennas and Related Literature

In recent years, reconfigurable antennas have widely been utilized in various wearable applications. A reconfigurable antenna is an antenna of which the radiation characteristics can be manipulated according to the altering environmental conditions [21]. The reconfiguration of the characteristics is achieved by deliberately changing the distribution of the currents on the radiating aperture of the antenna. The currents can be redistributed over the aperture using different methods such as altering the feeding, altering the physical structure of the antenna or altering the radiating edges [22]. The redistribution of the currents leads to a change in the electromagnetic fields on the aperture of the antenna, which ultimately changes its parameters and functionalities. As radiation characteristics of reconfigurable antennas can be modified according to the

changes in surrounding conditions, they provide a practical solution to the challenges encountered in wearable antenna design [23].

The techniques to reconfigure antenna characteristics are mainly classified into four different categories as shown in Figure 2.8 [24]. Electrically or optically reconfigurable antennas utilize a switching mechanism that makes use of one of the elements listed in Figure 2.8 to provide reconfiguration, whereas mechanically reconfigurable antennas achieve reconfiguration with a change in their physical structure and material reconfigurable antennas make use of smart materials such as ferrites and liquid crystals [22].

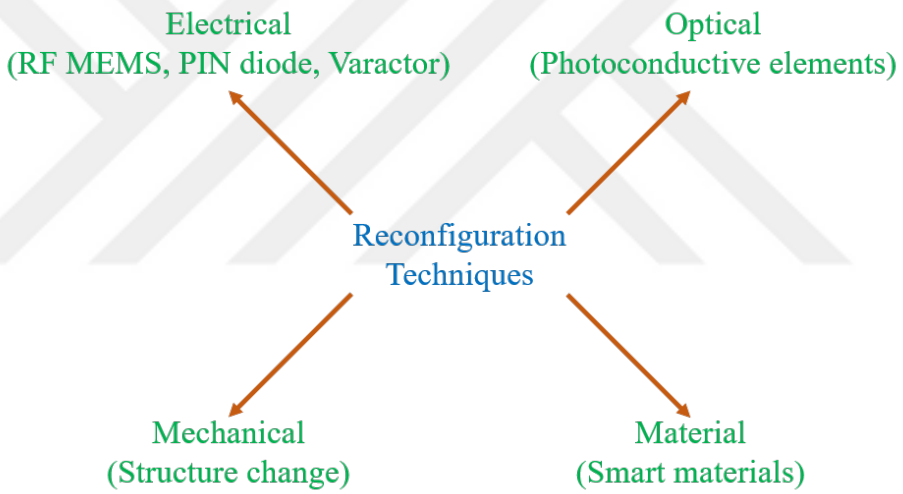

Figure 2.8. Different reconfiguration techniques.

The reconfiguration of radiation characteristics can take place in four different forms. A reconfigurable antenna can have a reconfigurable operating frequency, a reconfigurable radiation pattern, reconfigurable polarization or a combination of any of these three characteristics [21]. The types of reconfiguration are detailed in the next three subsections along with various designs proposed in the literature.

2.3.1. Frequency Reconfiguration

In frequency reconfiguration, the operating frequency of the antenna is changed, for example it is moved from 1.8 GHz to 2.4 GHz, by creating a tuning in the reflection coefficient [22]. The reconfiguration of the operating frequency can provide various performance improvements in wearable wireless systems, such as reduced interference with other systems or enhanced throughput [25].

In the literature, several designs that achieve frequency reconfiguration have been proposed. In [25], a textile antenna that can operate at six different frequencies from 1.57 GHz to 2.55 GHz by using three PIN diodes to adjust the slot length is presented. In [26], a flexible antenna consisting of a folded slot and a stub that can be manipulated with a PIN diode to provide two distinct operating frequencies is proposed. A fluidic microstrip monopole antenna that uses substrate milled channels filled with either air or distilled water to change its operating frequency is designed in [27]. In [28], a frequency reconfigurable fabric patch antenna that is tuned by means of two varactor diodes is reported. Finally in [29] and [30], two different frequency reconfigurable patch antennas operating in the 5G frequency bands are designed on LCP and PET substrates, respectively.

2.3.2. Polarization Reconfiguration

A polarization reconfigurable antenna has the ability to change its polarization from one type to the other, e.g. from horizontal to right-hand circular polarization [22]. The main purpose of polarization reconfiguration is to prevent the power loss caused by the polarization mismatches between the transmit and receive antennas that stem from a change in the position or orientation of the antennas introduced by the mobility of humans [31].

A number of polarization reconfigurable antennas have been proposed in the literature. In [31], a textile patch antenna providing three polarization modes for

wearable IoT applications is proposed. In [32], a U-slot patch antenna that achieves polarization reconfiguration by altering the length of the U-slot arms by means of two PIN diodes is presented. A square slot antenna with a compact CPW feed that has two ports excited separately to achieve two polarization modes is designed in [33]. Similarly in [34], a square slot fed by a CPW feeding structure that is manipulated via two PIN diodes to provide horizontal and vertical polarization is reported. Finally, a polarization reconfigurable square patch antenna with a T-shaped feed is proposed in [35].

2.3.3. Pattern Reconfiguration

A pattern reconfigurable antenna is an antenna that is able to tune or change its radiation pattern in terms of shape, direction or gain [22]. To illustrate, pattern reconfiguration may include steering the direction of maximum radiation or placing the null of the pattern at a specific location [36]. The overall performance of a wireless system can greatly be enhanced by the utilization of pattern reconfigurable antennas [37]. Particularly, pattern reconfiguration can be useful in terms of increasing the probability of getting a reliable link in wearable applications as the direction of arrival changes over time due to the mobility of the users. In such a case, the pattern can be switched between predefined patterns in order to find the one that supports the best link quality [20]. Conventionally, arrays are utilized to reconfigure the radiation pattern. However, as the size is restricted in wearable applications as mentioned in Section 2.2, utilization of arrays is not suitable. Thus, a wearable application can greatly benefit from an antenna that replaces two or more antennas to achieve pattern diversity [36].

There are various pattern reconfigurable antennas proposed in the literature. In [20], [38] and [39], antennas that achieve pattern reconfiguration by a manipulation in their feedlines via switches are presented. Antennas proposed in [40] and [41] have two ports excited separately to create two different modes providing pattern diversity without switches. Similarly in [42], the authors present a switchless antenna with two

separate ports excited simultaneously, where pattern reconfiguration is achieved by applying a phase shift between the ports. The patch antennas proposed in [43], [44] and [45] can be operated in either monopolar patch or normal patch modes by means of PIN diodes used to short-circuit the patch and the ground plane. The ground planes of the patch antennas reported in [46] and [47] are modified with artificial switches to provide pattern diversity. An antenna that can operate either as a monopole or a slot according to the states of the switches and hence creates two different radiation patterns is presented in [48]. Finally in [49], the slits positioned symmetrically around the slot are manipulated via PIN diodes to provide pattern diversity.

2.4. Novelty of the Proposed Design and a Comparison with Existing Designs

As mentioned in Section 1.2, the proposed antenna is a pattern and polarization reconfigurable wearable slot antenna that is fed by a single CPW feed and switched between two modes of operation via PIN diodes. The proposed design mainly differs from the literature in two ways. Firstly, pattern reconfiguration is achieved by generating two distinct modes of operation from a single slot; while in the literature, pattern reconfiguration is frequently provided by manipulating the feedline of the antenna [20, 39], or connecting new elements to the main radiating aperture [43, 44], or to the ground plane [46,47]. Secondly, glass is used as the substrate of the proposed antenna; whereas conventionally, along with standard substrates such as FR4-Epoxy [40,44], flexible substrates [38, 47] are exploited as the substrate of wearable pattern reconfigurable antennas. To the author's knowledge, there is no pattern reconfigurable wearable antenna designed on glass.

Some of the polarization or pattern reconfigurable antennas mentioned in Subsection 2.3.2 and Subsection 2.3.3 are slot antennas [33,34,39,41,48,49]. Among these, [33] and [41] comprise of multiple ports that are excited separately and the reconfiguration is provided by port selection. Therefore, the proposed antenna differs from the designs proposed in [33] and [41]. [34], [39], [48] and [49] can achieve reconfiguration with a sin-

gle port. However, [34] and [39] differ from the proposed antenna in the fact that they achieve reconfiguration by manipulating their feedlines. Furthermore; [34], [39], [48] and [49] are not intended and thus not suitable for wearable applications due to their large dimensions. Elaborately, [34] and [39] have large electrical sizes of $0.69\lambda_0 \times 0.56\lambda_0$ and $0.83\lambda_0 \times 0.83\lambda_0$, respectively, and [48] and [49] have thick profiles of 7.2 mm (2.3 - 2.4 GHz) and 4.5 mm (1.8 - 2.1 GHz), respectively.

A comparison in terms of four main properties between the proposed antenna and related reconfigurable antennas in the literature mentioned in the previous subsections is provided in Figure 2.9. As can be seen, there is no other antenna that is wearable, pattern or polarization reconfigurable, smaller than 4 cm × 4 cm and has a realized switching mechanism.

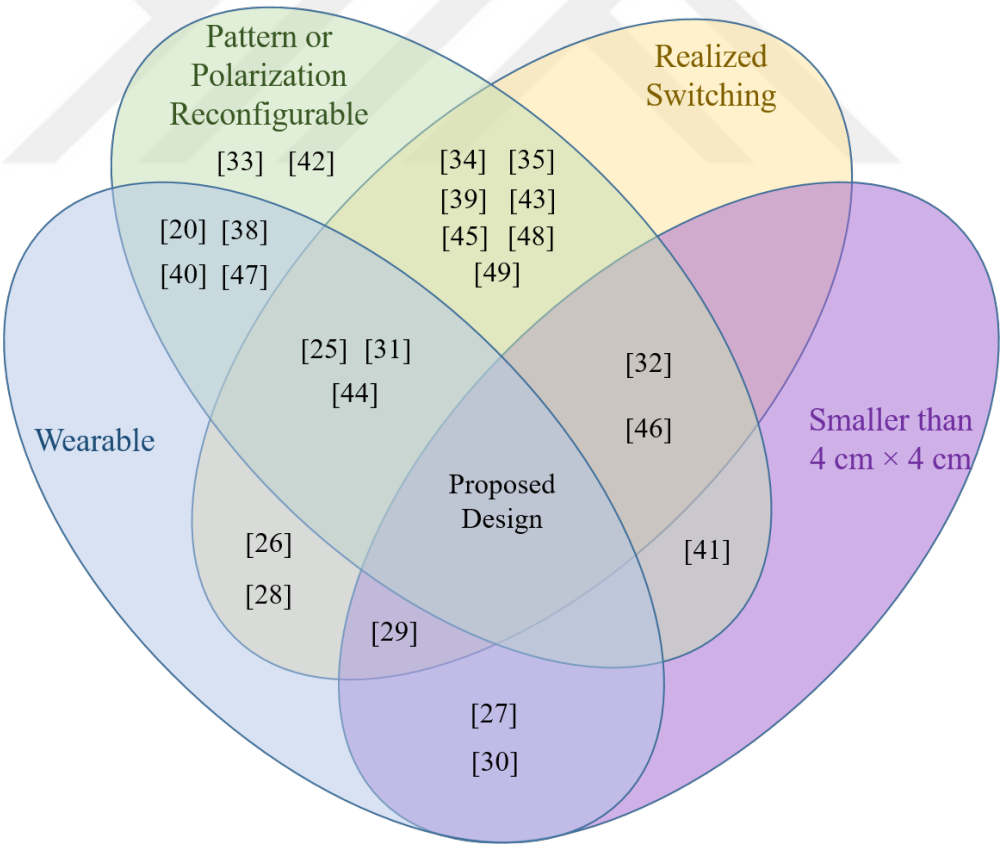

Figure 2.9. A comparison between the proposed antenna and related reconfigurable antennas in the literature.

3. PRELIMINARY MODELS

This chapter presents the first two antenna models developed to operate in the 2.4 GHz ISM band and discusses the reasons for the need for an optimized final model. The first model is a microstrip fed model that consists of two separate slots. This model is described in Section 3.1. The second model presented in Section 3.2 consists of two separate slots as well, whereas it is a cavity backed model fed by a stripline. Although there are several issues related to the operation or the design of these models, they form the basis of the approach used to design the optimized model presented in the next chapter.

3.1. First Model

3.1.1. The Antenna Model

In order to achieve the previously defined goals of pattern and polarization diversity, the main method employed in the first design is to etch two separate slots on a ground plane that are positioned in perpendicular to each other as shown in Figure 3.1. The perpendicular positioning allows the slots to have different polarizations as well as the nulls of the radiation patterns created by the slots to be placed in different positions in the azimuth plane. The slots are to be excited in an alternating way with a single meandered microstrip feed. As one of the slots is activated, the other one will be shorted by means of switches. Stated otherwise, the slot that is not to be excited is divided with a switch into two slots that are due to their shorter lengths resonant at higher frequencies than the intended operating frequency. Considering the ultimate goal of using the design in smart glasses, ideal glass ($\epsilon_r = 5.5$) that is 6 cm $\times$ 6 cm $\times$ 1 mm in size is used as the substrate of the antenna. In addition, an L-shaped ground plane that is placed along the two edges of the substrate is preferred so that the visibility through the glass is not obstructed.

The first slot (Slot #1) is oriented horizontally with respect to the ground and creates dominantly a vertical polarization. As of now, this slot will be referred to as the horizontal slot and the mode at which the horizontal slot is activated will be referred to as the horizontal mode. On the contrary, the second slot (Slot #2) is oriented vertically to the ground. It creates dominantly a horizontal polarization. This slot will be referred to as the vertical slot and the mode at which the vertical slot is activated will be referred to as the vertical mode.

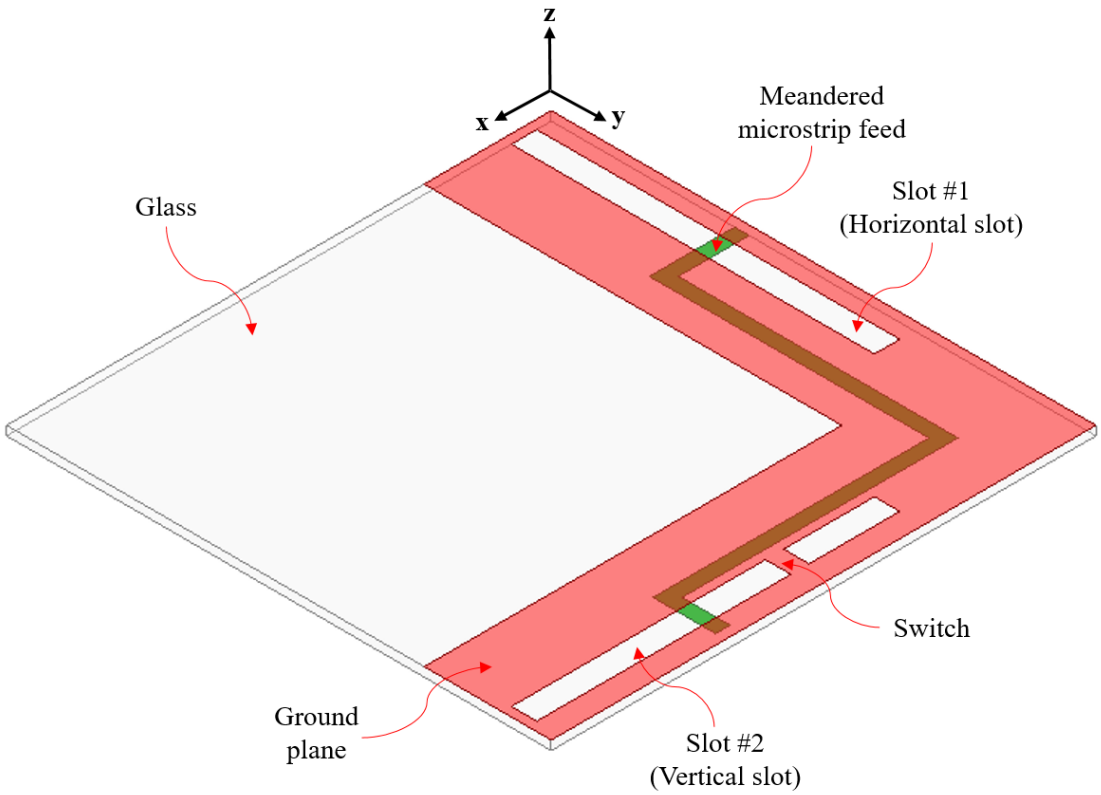

Figure 3.1. The microstrip fed slot antenna model.

3.1.2. Analytical Design

The parameters of the design that must be determined to optimize the performance of the antenna are visualized in Figure 3.2. Initially, the length and the width of the slots, the location of the feed with respect to the slots (feed offset) and the width of

the feed are analytically calculated using a narrow slot assumption. The results of the analytic calculation will later be used as the initial values of the numerical optimization. Firstly, considering the fact that the antenna is designed on a dielectric material,

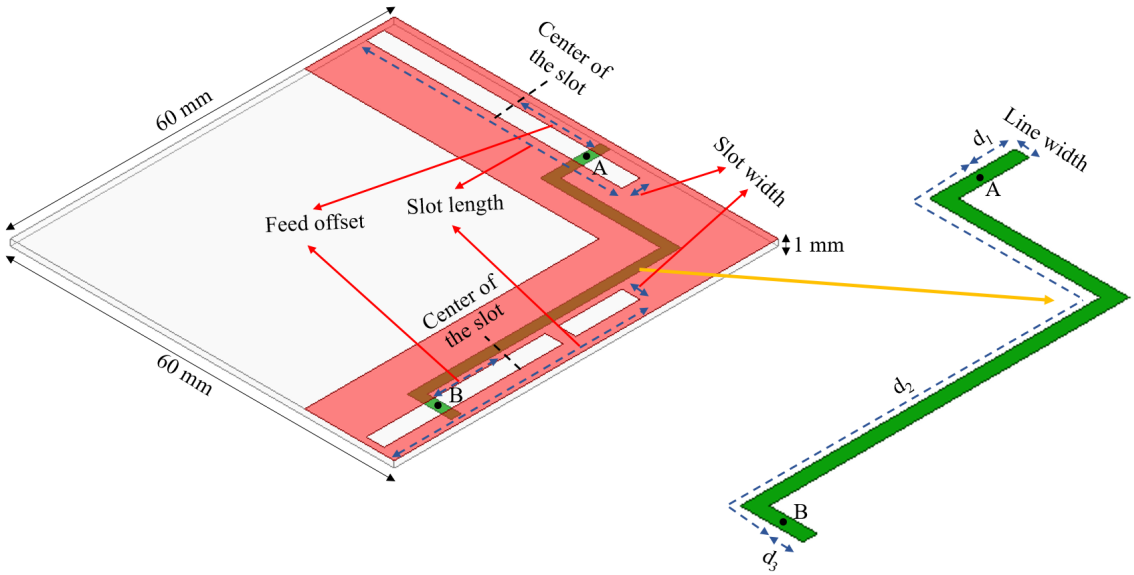

Figure 3.2. The parameters to be determined to optimize the performance of the microstrip fed antenna.

the length of the slots can be calculated as described in Subsection 2.1.3. The formulas required for length calculation are repeated here for convenience.

$$\epsilon_{eff} = \epsilon_r * ff + (1 - ff) \tag{3.1}$$

$$\lambda_g = \frac{\lambda_0}{\sqrt{\epsilon_{eff}}} \tag{3.2}$$

$$L = \frac{\lambda_g}{2} \tag{3.3}$$

The filling factor is a parameter that particularly depends on the structure of a specific antenna. According to the numerical studies conducted in BOUNTENNA Research Laboratory, the filling factor of a microstrip fed slot antenna at 2.45 GHz is determined to be around 0.3. Therefore, taking the filling factor as 0.3, the effective permittivity is calculated to be 2.35 using Equation 3.1. The free space wavelength at the center frequency (2.45 GHz) is calculated as 122.45 mm using

$$\lambda_0 = \frac{c}{f_0} \tag{3.4}$$

where c is the speed of light in free space. Therefore, the guided wavelength is calculated to be 79.88 mm using Equation 3.2 and the length of the slots is calculated to be 39.94 mm using Equation 3.3. Finally, as mentioned in Subsection 2.1.1, a thin slot can have a slot width of $\lambda_g/50$ which equals to 1.6 mm in the case the guided wavelength is 79.88 mm.

As for the calculation of the feed location, the slot is considered to be the dual of a half-wave dipole as described in Subsection 2.1.2. This means that the slots must be fed $\lambda_g/5$ away from their centers to match them to 50 Ω, which is approximately 15.98 mm.

Finally, the characteristic impedance of a microstrip line is given as

$$Z_0 = \frac{120\pi}{\sqrt{\epsilon_{eff(m)}}\left[\frac{W}{H} + 1.393 + \frac{2}{3}ln(\frac{W}{H} + 1.444)\right]} \tag{3.5}$$

where W is the width of the line, H is the thickness of the substrate and $\epsilon_{eff(m)}$ is the effective permittivity for the microstrip line which differs from the one for the slot and given as

$$\epsilon_{eff(m)} = \frac{\epsilon_r + 1}{2} + \frac{\epsilon_r - 1}{2\sqrt{1 + 12\left(\frac{H}{W}\right)}} \tag{3.6}$$

Taking the characteristic impedance of the line as 50 Ω, the width of the microstrip line is calculated to be 1.6 mm. Other parameters related to the feed line will be detailed in the next subsection.

3.1.3. Numerical Optimization

Before optimizing the model through numerical analysis, the equivalent circuit of the model must be detailed. The equivalent circuit of the model can better be understood by firstly considering the equivalent circuit of a single microstrip fed slot antenna as given in Figure 3.3 [50]. In the equivalent circuit, a transformer with a mutual inductance M, a primary winding self-inductance L_1 and a secondary winding self-inductance L_2 is used to present the coupling between the slot and the microstrip line. The calculation of these parameters can be found in [50]. As mentioned in Section 2.1, the radiation resistance (R_{rad}) of the slot is dependent on the feed offset. However, as can be seen in Figure 3.3, the impedance value resulting from the open circuit (Z_{OC}) is connected in series with the load impedance (Z_L) resulting from the radiation resistance. This impedance value depends on d_2, which is eventually one of the parameters that affect the input impedance seen from the feed. The input impedance also depends on d_1; hence, these parameters are critical in impedance matching of the slot. Similarly, if the reflections from the right angles on the feed line are ignored, the equivalent circuit of the first model for two modes of operation can be modeled as given in Figure 3.4. As can be observed from the equivalent circuit, the lengths of the different sections of the feed line (d_1, d_2, d_3) will have an effect on the input impedance of both slots. To ease the optimization process, the slots are placed such that d_2 equals to half a wavelength on the microstrip line at the operating frequency; that is, this microstrip line section behaves as an impedance repeater. In this way, it is ensured that the impedance value connected in series with the load impedance in the vertical mode will be the same as the one in the horizontal mode. Notice that the guided wavelength for the microstrip line will differ from the one for the slot. It is

calculated to be 61.07 mm at 2.45 GHz using

$$\lambda_g = \frac{\lambda_0}{\sqrt{\epsilon_{eff(m)}}} \tag{3.7}$$

which means that d_2 must be around 30.54 mm. The values of d_1 and d_3 are determined through numerical analysis.

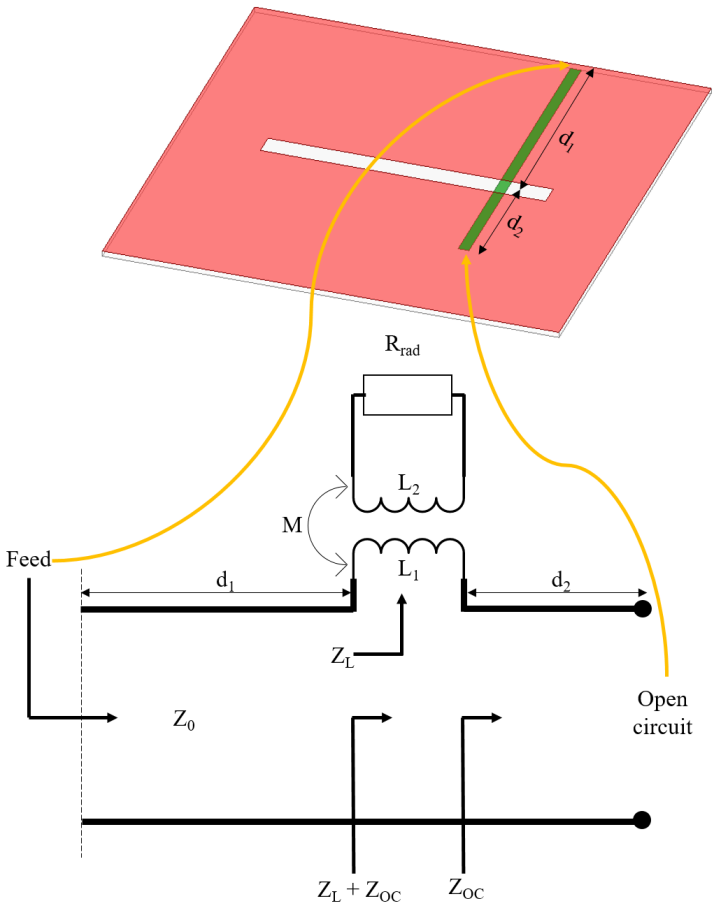

Figure 3.3. The equivalent circuit of a single microstrip fed slot antenna.

The model is implemented with the calculated values in ANSYS High Frequency Structure Simulator (HFSS) [51]. In HFSS; a lumped port is used for excitation, the terminal method is used as the solution type and an open region is used as the surrounding radiation region. Beginning from the calculated values, the parametrized dimensions of the antenna and the feed line are optimized. The frequency adjustment

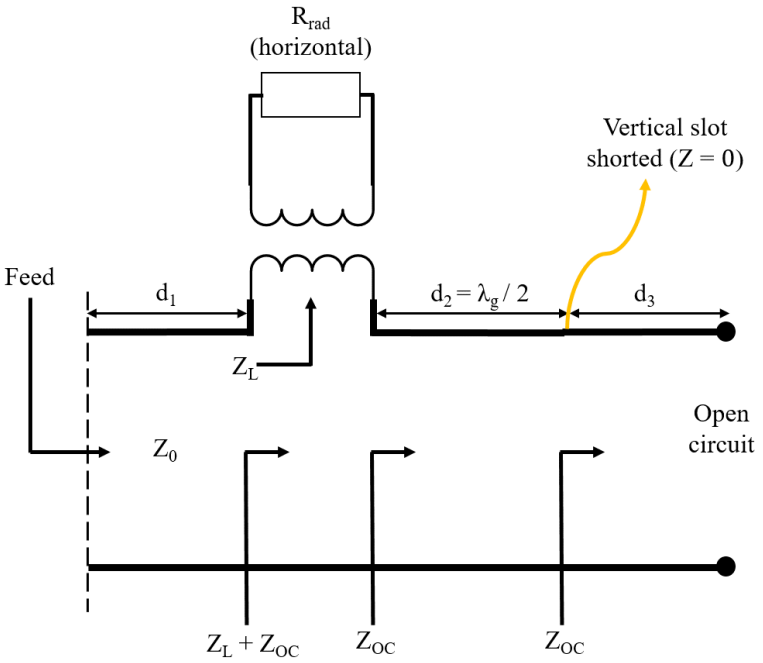

(a)

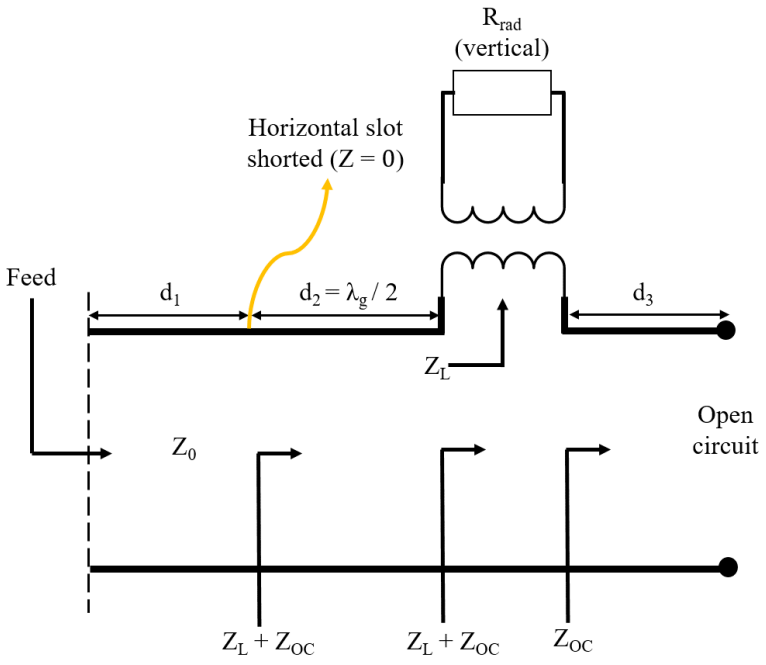

(b)

Figure 3.4. The equivalent circuit of the first model for two modes of operation (a) the horizontal mode (b) the vertical mode.

is substantially achieved by changing the length of the slots, whereas the matching is provided by changing the dimensions of the feed line and thus the feed position of the slots. However, note that even though it is not as crucial as the effect of the slot length, the position of the feed has also an effect on the operating frequency. The optimized values are tabulated along with the calculated ones in Table 3.1.

Table 3.1. The calculated and optimized values of the parametrized dimensions for the first model.

	Calculated Values (mm)	**Optimized Values (mm)**
Slot Length	39.94	40
Slot Width	1.6	2.2
Feed Offset (Horizontal)	15.98	19
Feed Offset (Vertical)	15.98	15
Line Width	1.6	1.6
$\mathbf{d}_1$	-	4
$\mathbf{d}_2$	30.54	33.5
$\mathbf{d}_3$	-	1.9

3.1.4. Results and Discussion

Figure 3.5 shows the simulated frequency response of the first model for two modes of operation in air. The corresponding center frequency and the magnitude of the reflection coefficient are tabulated in Table 3.2. It can be noticed that the model is operating in the desired frequency band and the center frequencies of two modes agree. Moreover, the return loss is greater than 10 dB for both modes of operation.

Although the model seems to operate as desired according to the frequency response, a problem arises when the radiation patterns are studied. Simulated 3D radiation patterns and 2D radiation patterns at $\phi = 0°$ and $\theta = 90°$ at the operating

Table 3.2. The center frequency and the magnitude of the reflection coefficient for the first model in air.

	Center Frequency (GHz)	$\|s_{11}\|$ **(dB)**
Horizontal Mode	2.43	-28.82
Vertical Mode	2.42	-13.36

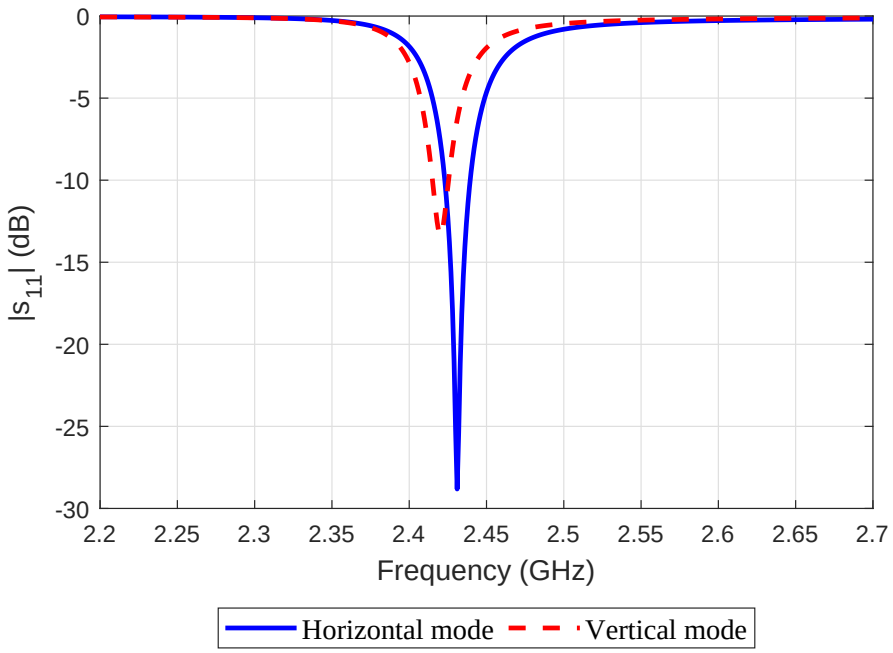

Figure 3.5. Simulated frequency responses of the first model in air.

frequency for the horizontal and vertical mode in air can be seen in Figure 3.6 and Figure 3.7, respectively. For the ease of comparison, the patterns are given along with the standard bidirectional patterns that are expected to be created by a slot antenna aligned in the same direction as the corresponding mode. The maximum gains are 4.3 dBi and 4.6 dBi for the horizontal and vertical mode, respectively. However, it is observed that when compared with the standard ones, the radiation patterns created by the model have distortions. These distortions are observed more intensely in the azimuth plane and are estimated to be caused by the radiation from the feed line. This estimation can be validated by examining the electric field distribution on the antenna and the feed line as given in Figure 3.8. The electric field distribution on

the feed line shows that the feed line also radiates in both modes of operation. It is actually expected that the radiation patterns are affected by the radiation from the feed line as a microstrip line is an unclosed structure. However, the radiation from the feed line is at a non-negligible level and has an unpredictably large effect on the patterns as it is an electrically long line containing many discontinuities (sharp corners and the open-circuited end). In other words, the patterns are more heavily distorted by the radiation from the feed line than expected due to its complex structure. It is an undesired result since, besides the distortions, it also leads to loss of power from the feed line. Therefore, the model must be modified such that the distortions caused by the radiation from the feed line are eliminated. Due to this problem faced during the simulations, this model has never been prototyped and measured. Note that, even though there are distortions in the radiation patterns, it can be observed from the 2D patterns given in Figure 3.6(c) and Figure 3.7(c) that the pattern is rotated between two modes of operation. This indicates that pattern reconfiguration can be achieved with the employed method.

3.2. Second Model

3.2.1. The Antenna Model

Recall that the main drawback of the first design was the unintended radiation from the feed line and its effect on the radiation patterns. To overcome this issue, the second model developed is a cavity backed slot (CBS) antenna fed by a stripline as shown in Figure 3.9. The cavity ensures the removal of the undesired effects caused by the feed line as it is totally enclosed by metal surfaces that provide a high degree of isolation such that the RF signals on the stripline are less likely to interfere with the external signals [52]. The design approach to provide pattern and polarization diversity is quite similar to the first design. Two separate slots (horizontal and vertical) that are perpendicular to each other are etched onto the cavity. The cavity is an L-shaped shallow cavity that has a thickness of 2.54 mm and is filled with Rogers RO3210 laminate [53] with a relative permittivity of 10.2. Again, the slots are excited in an

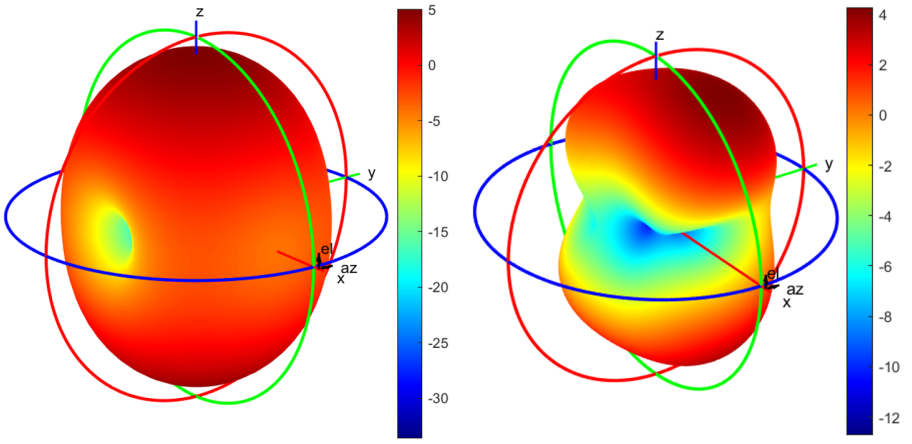

(a)

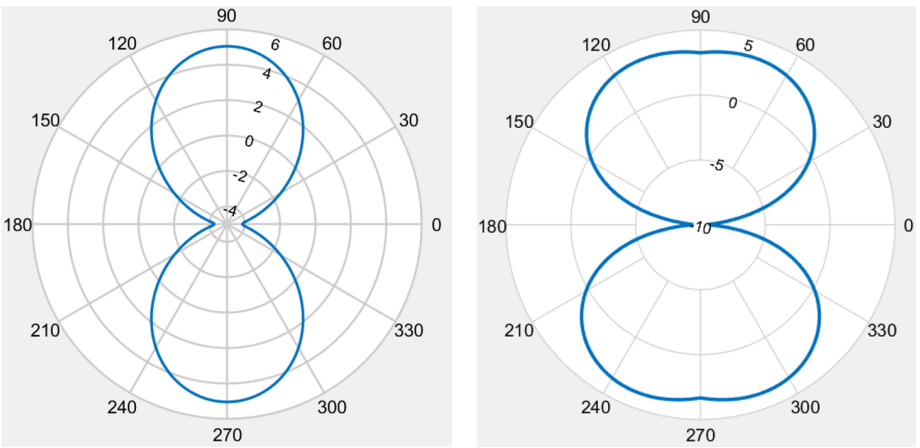

(b)

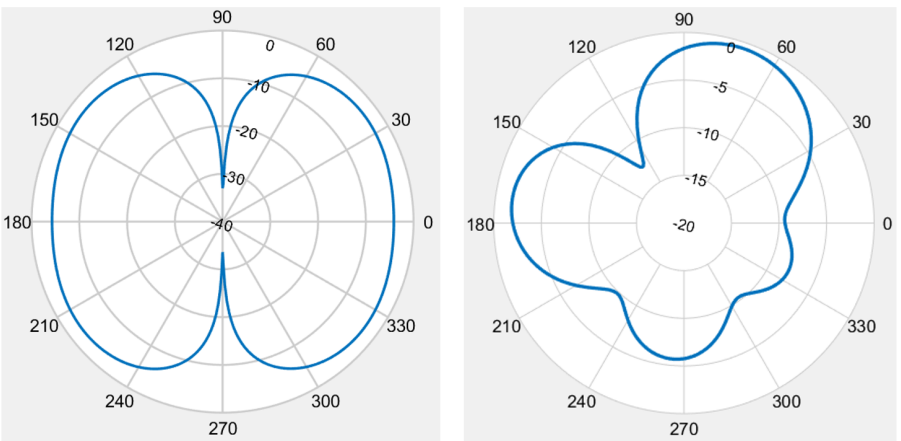

(c)

Figure 3.6. The standard bidirectional radiation pattern of a horizontally aligned slot antenna (left) and the simulated radiation pattern of the horizontal mode (right) (unit: dBi) (a) 3D patterns (b) 2D patterns at $\phi = 0°$ (c) 2D patterns at $\theta = 90°$.

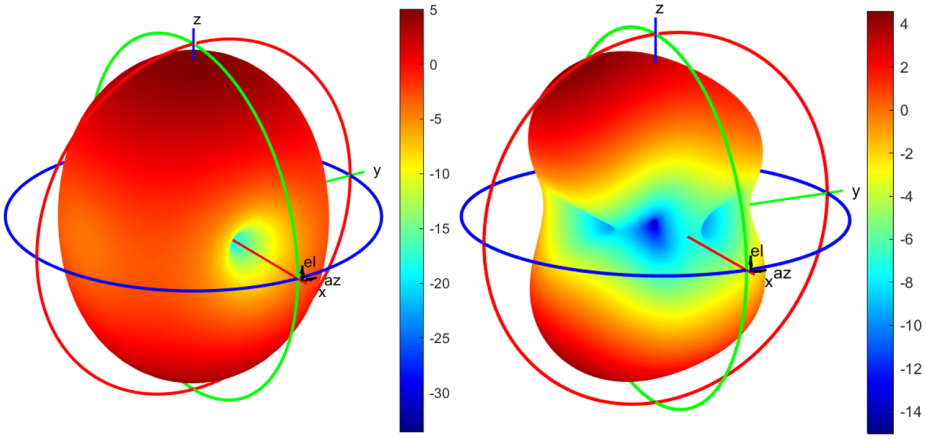

(a)

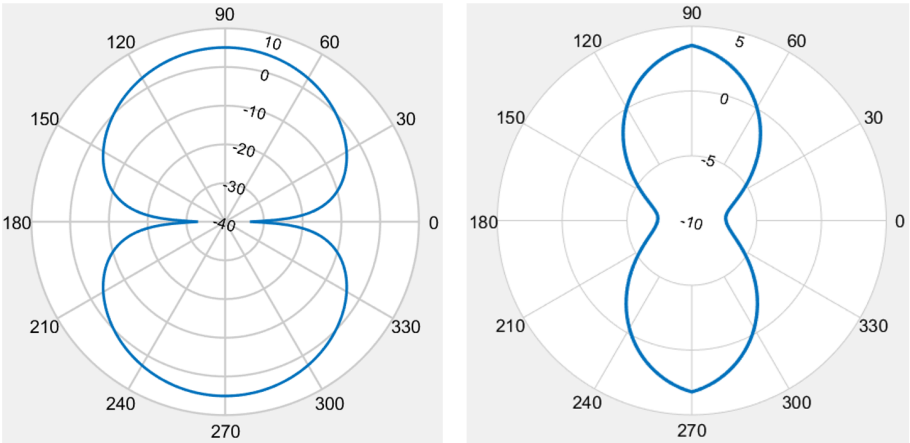

(b)

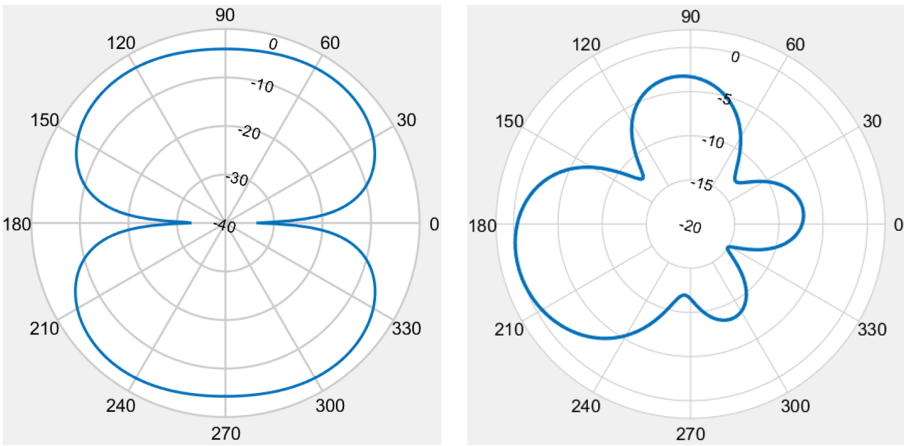

(c)

Figure 3.7. The standard bidirectional radiation pattern of a vertically aligned slot antenna (left) and the simulated radiation pattern of the vertical mode (right) (unit: dBi) (a) 3D patterns (b) 2D patterns at $\phi = 0°$ (c) 2D patterns at $\theta = 90°$.

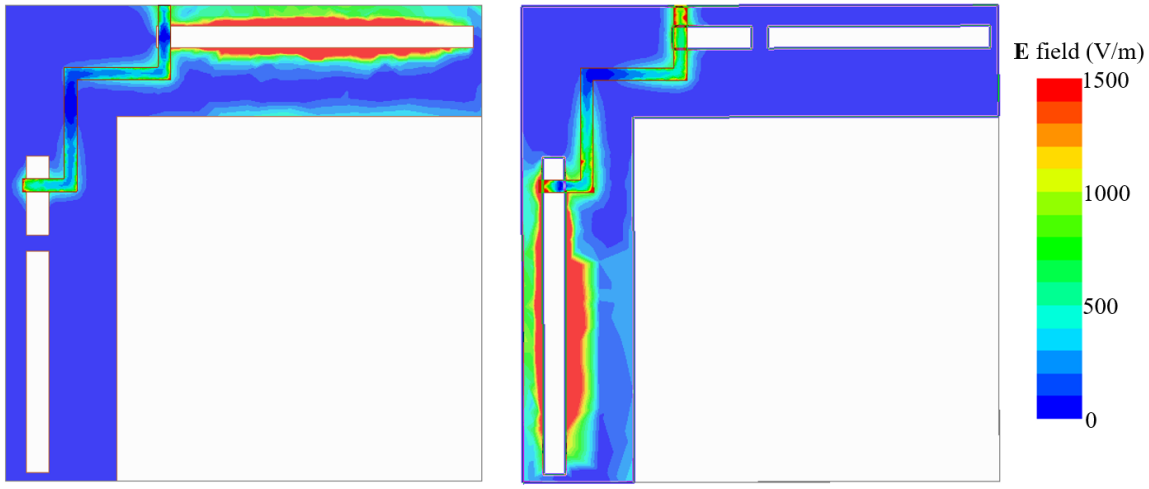

Figure 3.8. The electric field distribution on the antenna and the feed line for the horizontal (left) and vertical (right) mode.

alternating way by means of switches. However, unlike the first model, the feeding structure here is a stripline without sharp corners that is sandwiched between two 1.27 mm thick Rogers RO3210 substrates. The structure of the feed line will be detailed in Subsection 3.2.3.

3.2.2. Analytical Design

The parameters of the design that must be determined to optimize the performance of the antenna are visualized in Figure 3.10. For the analytical design, it is possible to neglect the interaction between the cavity modes and the fundamental slot mode, as the resonant frequencies of the slots are primarily determined by the lengths of the slots rather than the size of the cavity. Therefore, the same approach as in Subsection 3.1.2 can be used to calculate the dimensions of the slots. It is accepted as a good estimation to take the filling factor as 0.1 for CBS antennas [54]. Taking the filling factor as 0.1, the effective permittivity is calculated to be 1.92 using Equation 3.1. The guided wavelength at 2.45 GHz is calculated as 88.37 mm using Equation 3.2, which means that the length and the width of the slots should be 44.19 mm and

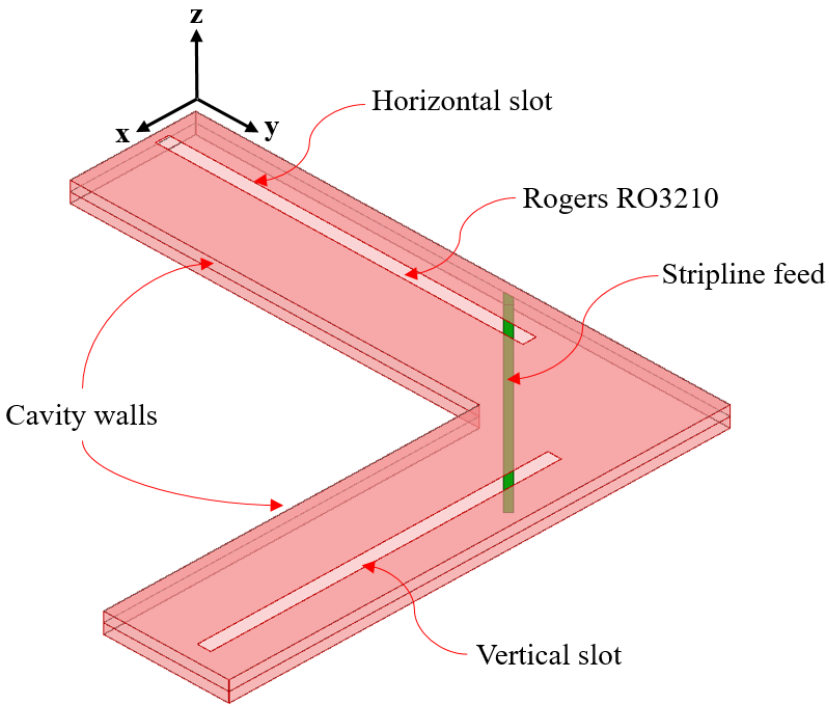

Figure 3.9. The cavity backed slot antenna model.

1.77 mm, respectively. The characteristic impedance of a stripline can approximately be calculated by

$$Z_0 = \frac{60}{\sqrt{\epsilon_r}} ln\left(\frac{3.8H}{0.8W}\right) \tag{3.8}$$

where H is the thickness of the substrate and W is the width of the stripline. Note that the relative permittivity of the material can directly be used to calculate the characteristic impedance. Contrary to the microstrip line, an effective permittivity is not required as the stripline is totally covered with the dielectric material. Given that the characteristic impedance of the line is 50 Ω, the required width is calculated to be 0.85 mm. As the Babinet's principle can not approximately be applied to CBS antennas, the feed offset values can not analytically be calculated [55]. They will be determined numerically along with the strip offset in the next subsection.

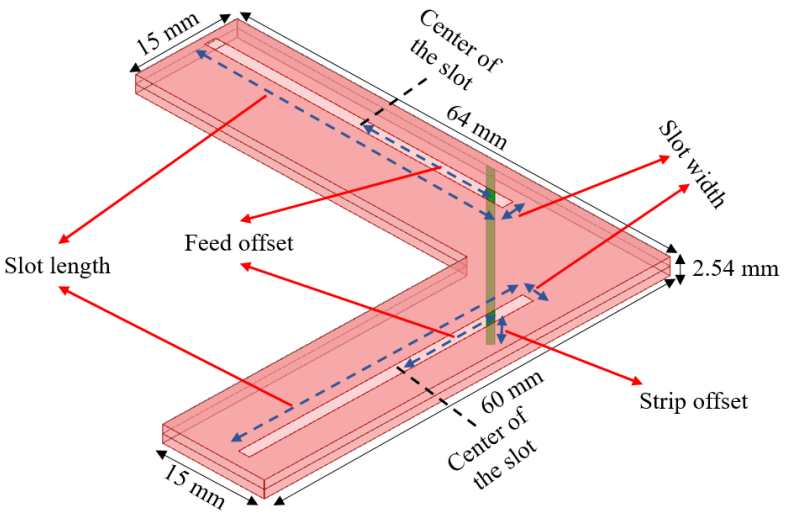

Figure 3.10. The parameters to be determined to optimize the performance of the CBS antenna.

3.2.3. Numerical Optimization and Prototyping

Before the parametrized values are optimized through numerical analysis, the equivalent circuit of the model must be detailed. The equivalent circuit of the second model for two modes of operation visualized in Figure 3.11 is similar to the one of the first model. Recall that the impedance resulting from the open circuit affects the matching of both slots. As it is done in the first model, the slots are placed such that the length of the stripline section between the slots is half a wavelength on the stripline at the operating frequency. Note that the guided wavelength for the stripline will differ from the one for the slot as the stripline is totally enclosed by the dielectric material. The guided wavelength for the stripline at 2.45 GHz is calculated to be 38 mm using Equation 3.9; hence, the length of the stripline section between the slots should be 19 mm.

$$\lambda_g = \frac{\lambda_0}{\sqrt{\epsilon_r}} \tag{3.9}$$

Firstly, the horizontal slot is shorted and the vertical slot is optimized by numerically determining optimum values for the feed offset of the vertical slot and the strip offset. Notice that modifying the feed offset values will not change the length of the stripline section between the slots, they only affect the radiation resistances of the slots. After the optimization of the vertical slot is completed, the horizontal slot is optimized with the vertical slot shorted. The optimized values are tabulated along with the calculated ones in Table 3.3.

In order to measure the frequency response of the model, the antenna is prototyped using two layers of 1.27 mm thick Rogers RO3210 substrates. The stripline feed and the edges of the slots are printed on the substrate by dispensing conductive ink with a conductivity of 1052632 S/m at DC using Voltera V-One [56]. The conductive ink is then cured at 200°C. Finally, the cavity walls are covered with copper tape. The completed prototype can be seen in Figure 3.12.

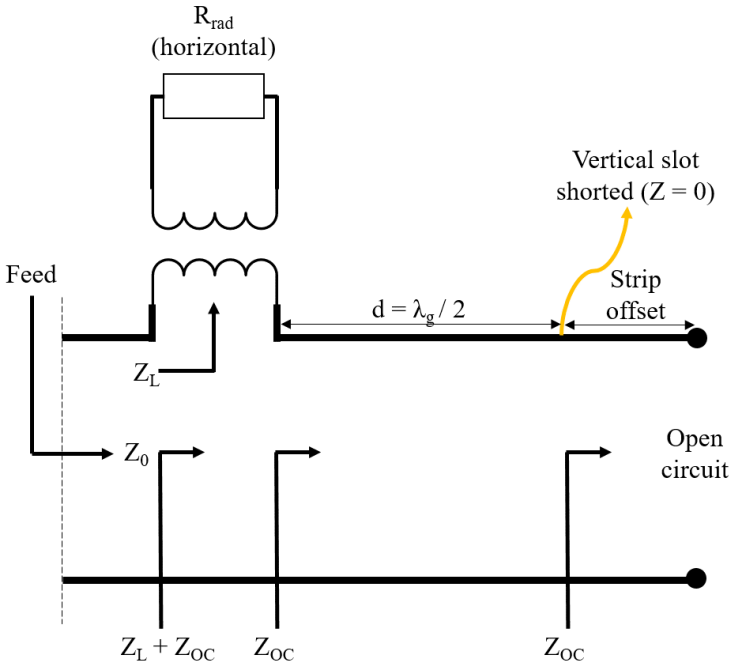

(a)

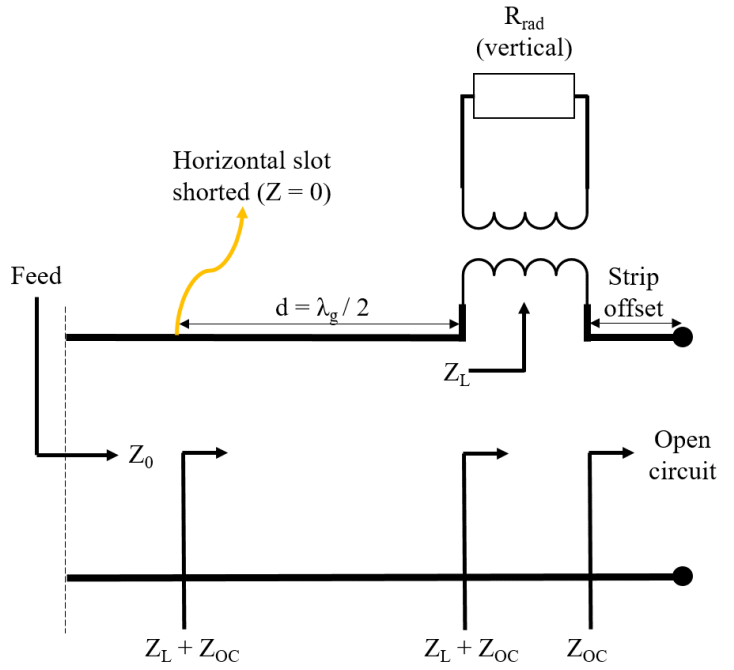

(b)

Figure 3.11. The equivalent circuit of the second model for two modes of operation (a) the horizontal mode (b) the vertical mode.

Table 3.3. The calculated and optimized values of the parametrized dimensions for the second model.

	Calculated Values (mm)	**Optimized Values (mm)**
Slot Length (Horizontal)	44.19	44
Slot Length (Vertical)	44.19	42
Slot Width	1.77	1.6
Feed Offset (Horizontal)	-	20.3
Feed Offset (Vertical)	-	16.3
Strip Offset	-	3.8

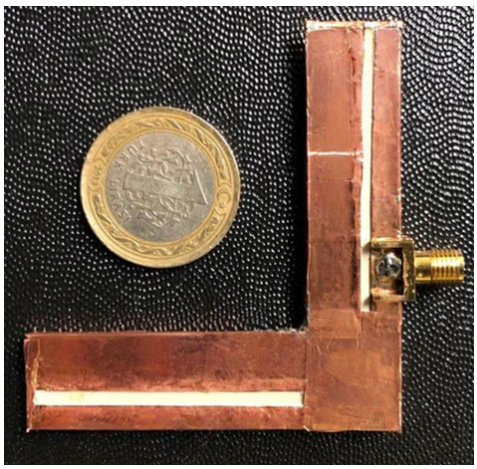

Figure 3.12. The prototype of the CBS antenna.

3.2.4. Results and Discussion

Figure 3.13 shows the simulated frequency response of the optimized model for two modes of operation in air. The corresponding center frequency and the magnitude of the reflection coefficient are tabulated in Table 3.4. It can be seen that the antenna is resonant at 2.44 GHz with a return loss greater than 10 dB for both modes of operation. Figure 3.14 shows the simulated 3D radiation patterns at 2.44 GHz for two modes of operation in air along with the 2D radiation patterns at $\phi = 0°$ and $\phi = 90°$. The position and the value of the maximum gain and the null are tabulated in Table 3.5. As can be seen, no distortions are observed in the radiation patterns as expected. Furthermore, it can be noticed that the polarizations of the patterns are perpendicular to each other and the position of the null is rotated between two modes of operation, which means that the intended pattern and polarization reconfiguration is accomplished with the employed method.

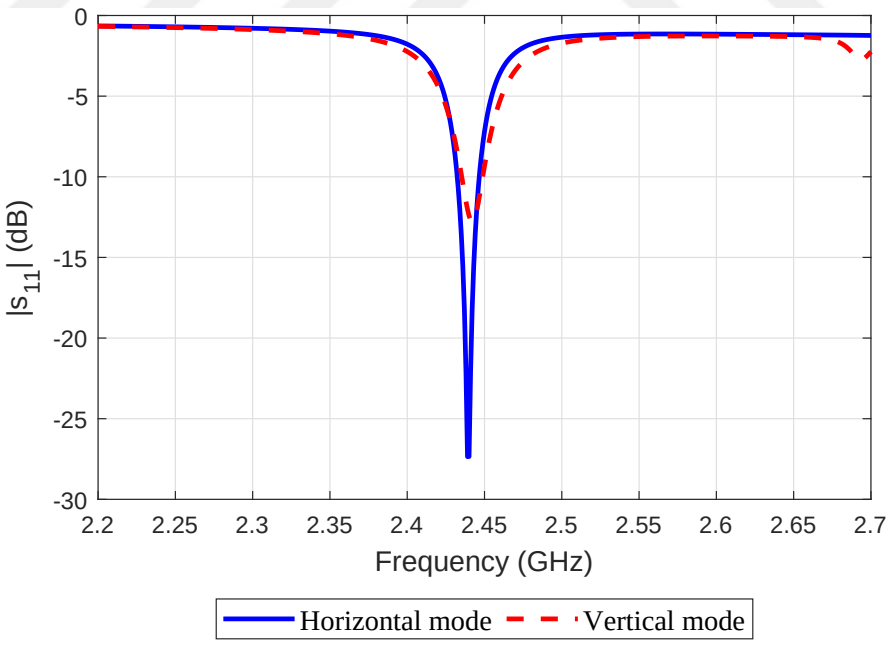

Figure 3.13. Simulated frequency responses of the second model in air.

Table 3.4. The center frequency and the magnitude of the reflection coefficient for the second model in air.

	Center Frequency (GHz)	$\|s_{11}\|$ **(dB)**
Horizontal Mode	2.44	-27.35
Vertical Mode	2.44	-12.79

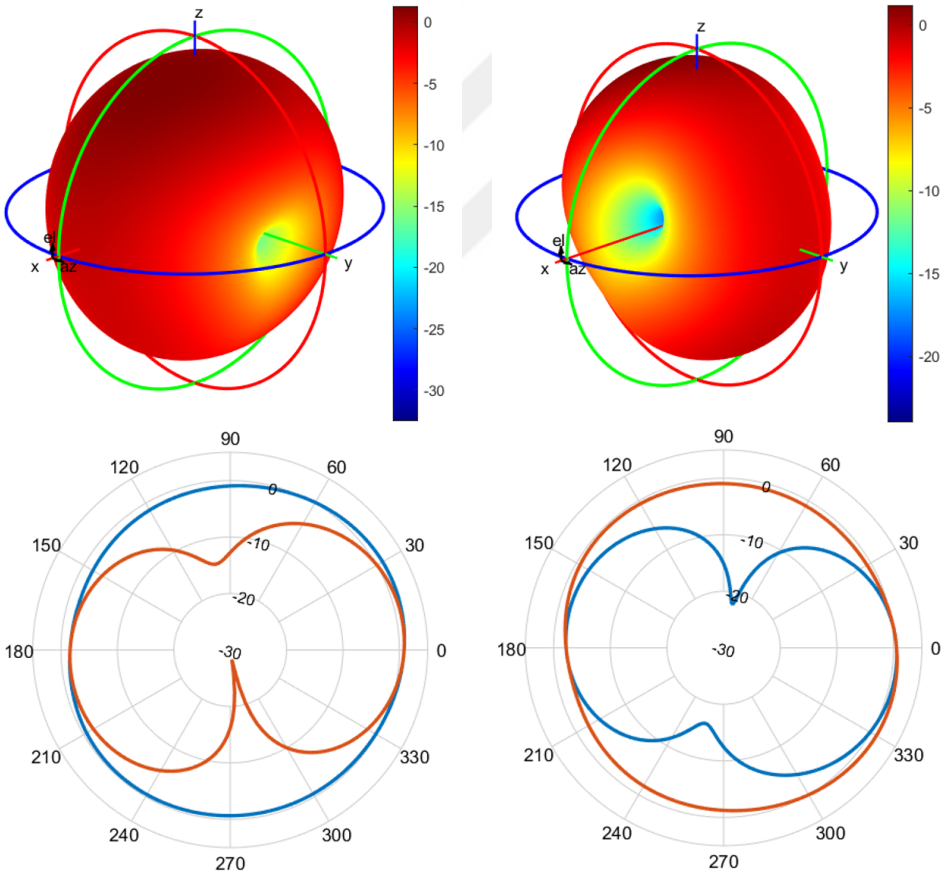

(a) (b)

Figure 3.14. Simulated 3D and 2D radiation patterns (Blue: $\phi = 0°$, Orange: $\phi = 90°$) of the second model (unit: dBi) (a) the horizontal mode (b) the vertical mode.

Table 3.5. The value and the position of the maximum gain and the null for the second model.

		Horizontal Mode	**Vertical Mode**
Maximum Gain	Value (dBi)	1.3	1.2
	Position	$\phi = 14^\circ$ $\theta = 20^\circ$	$\phi = -102^\circ$ $\theta = 24^\circ$
Null	Value (dBi)	-32.6	-24
	Position	$\phi = -92^\circ$ $\theta = 80^\circ$	$\phi = 4^\circ$ $\theta = 78^\circ$

The problem with this model is faced as the first prototype is measured. The measured frequency response of the first prototype for two modes of operation in air is labelled as horizontal mode 1 and vertical mode 1 in Figure 3.15. The corresponding center frequency and the magnitude of the reflection coefficient are given in Table 3.6. It can be noticed that the measured responses only partially agree with the simulation results. There is a shift in the resonant frequency of both modes. In addition, particularly for the horizontal mode, the measured return loss is not as reasonable as the estimated one. Both the detuning in the resonant frequency and the degradation in the matching are predicted to result from the imperfections during the prototyping process. The possible imperfections could be the separation between the two substrate layers which actually must be perfectly aligned, the unintentional gaps left on the cavity walls, the misalignment of the feed line with respect to the slots or the edges of the slots not being taped straightly. Therefore, the prototyping procedure explained above is repeated several times and each prototype is measured. However, although much care was given during prototyping, none of the measured frequency responses are satisfactory as can be seen from three measured frequency responses that are given as an example in Figure 3.15 and Table 3.6. The prototyping process can not be improved; hence, the model must be modified once again so that the prototyping can be performed more accurately. Note that as none of the measured frequency responses in air are satisfactory, the on-body performance of this model has never been evaluated.

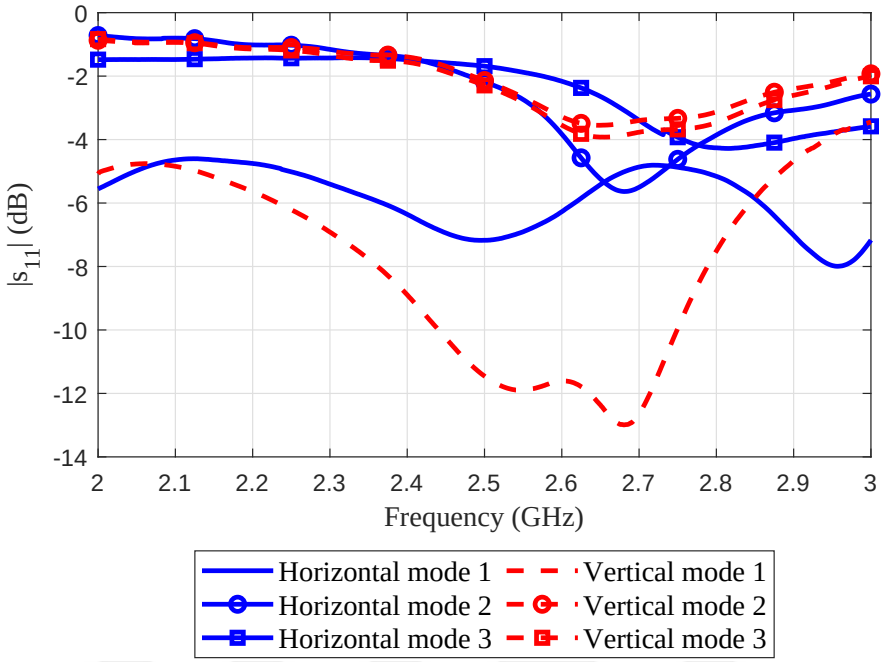

Figure 3.15. Measured frequency responses of the second model in air for three distinct prototypes.

Table 3.6. The measured center frequency and the magnitude of the reflection coefficient for three distinct prototypes of the second model.

	Center Frequency (GHz)	$\|s_{11}\|$ **(dB)**
Horizontal Mode 1	2.49	-7.18
Vertical Mode 1	2.54	-11.88
Horizontal Mode 2	2.67	-5.63
Vertical Mode 2	2.65	-3.55
Horizontal Mode 3	2.8	-4.27
Vertical Mode 3	2.65	-3.92

4. OPTIMIZED MODEL

This chapter presents the optimized final antenna model designed in the light of the results obtained from the preliminary models. Section 4.1 gives the general view and the operation principles of the antenna. In Section 4.2, the parametrized dimensions of the antenna are calculated analytically. These dimensions are optimized through numerical analysis in Section 4.3. Finally, the results in air are presented and discussed in Section 4.4.

4.1. The Antenna Model

Recall that the main drawback of the CBS antenna presented in Section 3.2 was that the imperfections during prototyping were leading to a shift in the resonant frequency and degradation in the matching in the measurements. To tackle this problem, the optimized model is designed to be fed by a CPW feed as shown in Figure 4.1. As can be understood from the word "co-planar", a CPW feed is located on the same side of the substrate with the ground plane. Hence, the alignment problem encountered in the CBS antenna can be eliminated with the use of the CPW feed. In addition, no cavity walls are required to eliminate the distortions caused by the feedline, as due to its small size, the radiation from the CPW feed is expected not to distort the radiation patterns. Contrary to two separate slots used in the preliminary models, a single equilateral L-shaped slot that consists of a horizontal and a vertical part is utilized in this model. The CPW feed is placed at the corner. Real glass ($\epsilon_r = 8.5$) used as the substrate is 35 mm $\times$ 35 mm $\times$ 1 mm in size. Similar to the preliminary models, two modes of operation, the horizontal mode and the vertical mode, are generated by means of switches. As can be seen in Figure 4.1, these two modes correspond to two L-shaped slots that are oriented in different directions. As these slots are oriented in different directions, they create patterns that are polarized in perpendicular to each other. The L-shaped slot with a longer horizontal part (horizontal mode) creates dominantly a vertical polarization, whereas the L-shaped slot with a longer vertical part (vertical

mode) creates a horizontal polarization. Notice that the position of the switches affects the length of the L-shaped slots as well as the position of the feed with respect to the slots and hence the impedance matching of the slots. Therefore, the position of the switches can not be chosen arbitrarily and must be taken into consideration during the design process.

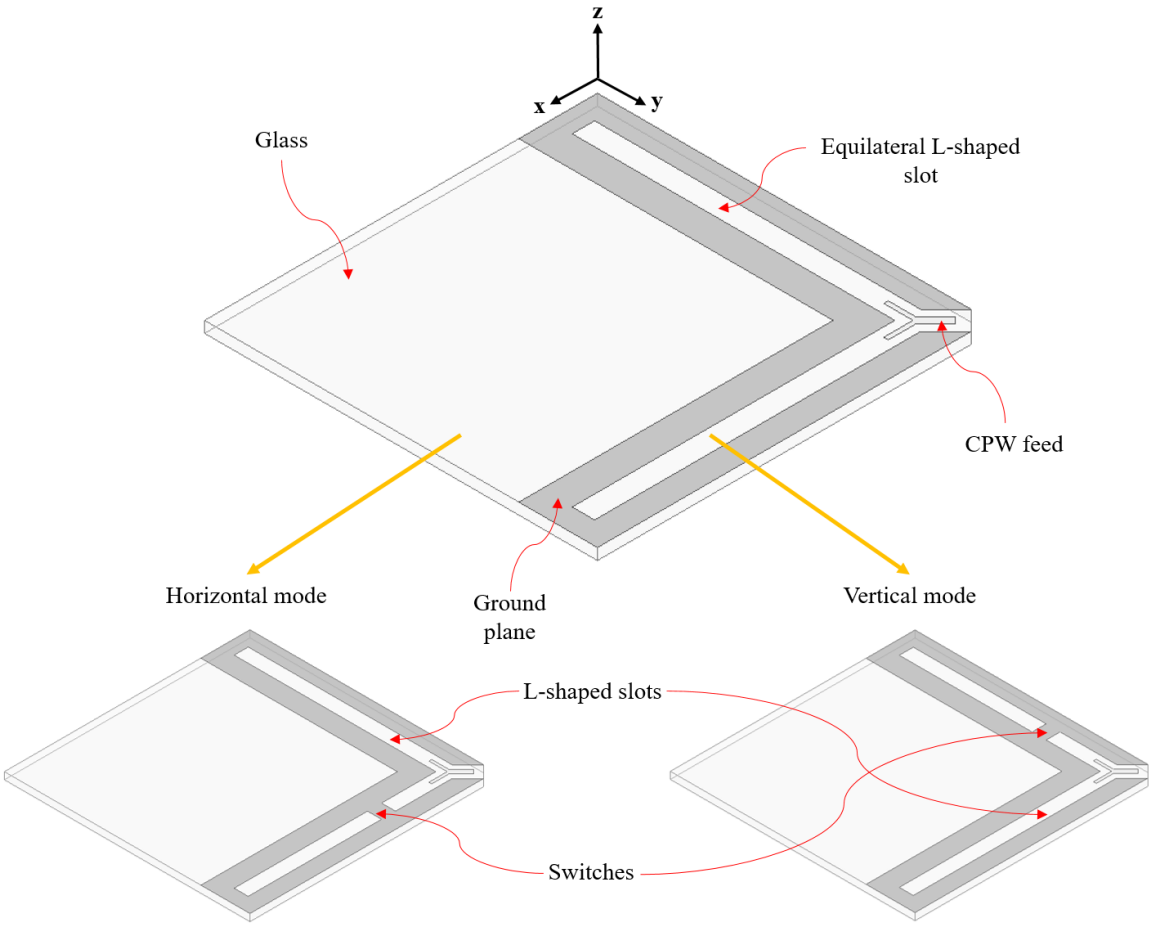

Figure 4.1. The optimized CPW fed slot antenna model.

4.2. Analytical Design

The parameters of the design that must be determined to optimize the performance of the antenna are visualized in Figure 4.2. As it is done in Chapter 3, the narrow slot assumption is used to analytically calculate the dimensions of the slots and

the results of the analytical calculation will be used as the initial values of the numerical optimization process. The required formulas are repeated here for convenience.

$$\epsilon_{eff} = \epsilon_r * ff + (1 - ff) \tag{4.1}$$

$$\lambda_g = \frac{\lambda_0}{\sqrt{\epsilon_{eff}}} \tag{4.2}$$

$$L = \frac{\lambda_g}{2} \tag{4.3}$$

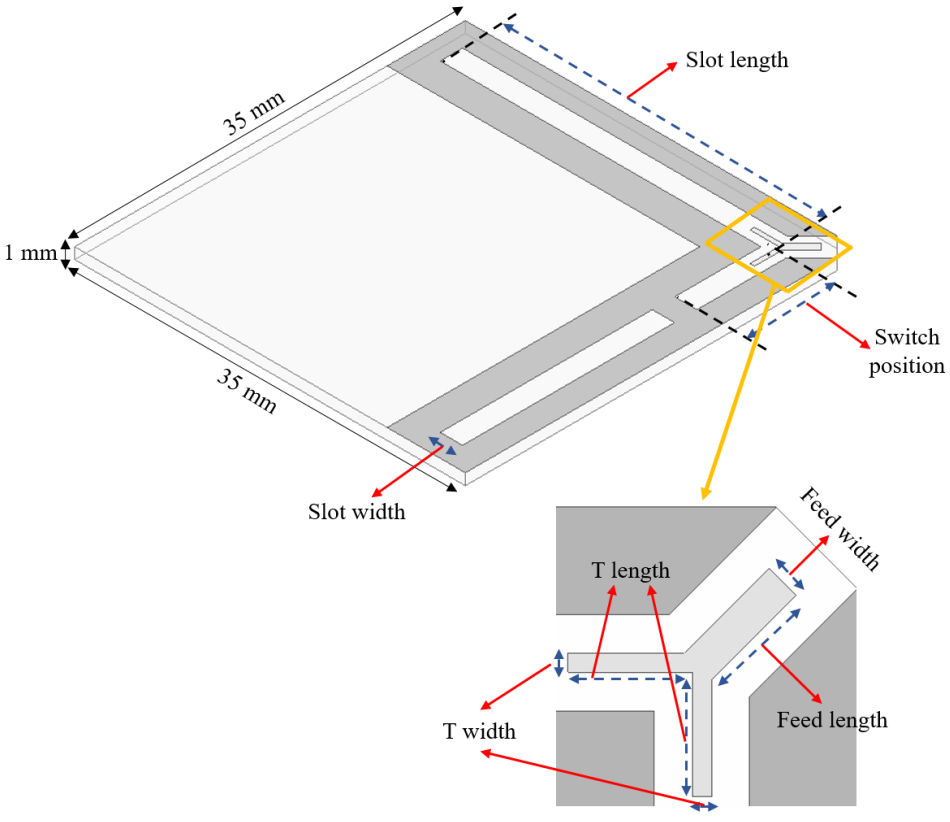

Figure 4.2. The parameters to be determined to optimize the performance of the CPW fed antenna.

As it is done in Section 3.1, the filling factor is taken as 0.3. Therefore, the effective permittivity is calculated to be 3.25 using Equation 4.1. The guided wavelength is calculated as 67.92 mm at 2.45 GHz using Equation 4.2, which means that the length and the width of the L-shaped slots must be 33.96 mm and 1.36 mm, respectively. Note that this length is the total length of the L-shaped slot. In order to determine the slot length value visualized in Figure 4.2, one must subtract the switch position from the total length.

As for the feed line, the characteristic impedance of the feed is mainly determined by the T-junction parameters visualized in Figure 4.2 as well as the thickness of the substrate since these parameters determine the capacitance and the inductance values of the distributed equivalent circuit. However, the equations governing the calculation of the capacitance and the inductance are rather complex and the computation approach is not straightforward [57]. Therefore, no analytical calculation is performed to determine the T-junction parameters and these parameters will be determined numerically in the next section. Nevertheless, an approximate position can be determined for the switches. As mentioned previously, the position of the feed with respect to the slots and thus the impedance matching of the slots is affected by the position of the switches. Recall that a slot must be fed $\lambda_g/5$ away from its center to match it to 50 Ω if it is considered as the dual of a dipole. Thus, the switch position is calculated to be 3.4 mm in the case the guided wavelength equals to 67.92 mm.

4.3. Numerical Optimization and Prototyping

Starting from the calculated values, the parametrized dimensions are optimized through numerical analysis in ANSYS HFSS. Note that the antenna is symmetrical with respect to its diagonal. This symmetry eases the optimization process as it ensures that when the performance of the antenna is optimized for one of the modes, its performance for the other mode is automatically optimized due to the fact that the two operation modes only differ in the orientation of the radiating L-shaped slot. The optimized values are tabulated along with the calculated ones in Table 4.1. The prototype of

Table 4.1. The calculated and optimized values of the parametrized dimensions for the optimized model.

	Calculated Values (mm)	**Optimized Values (mm)**
Slot Length	30.56	24.3
Slot Width	1.36	1.6
Switch Position	3.4	7.8
Feed Length	-	3.5
Feed Width	-	1.2
T Length	-	1.7
T Width	-	0.7

the optimized model can be seen in Figure 4.3. As it is done for the CBS antenna, conductive ink is dispensed on the glass substrate using Voltera V-One and cured at 200°C.

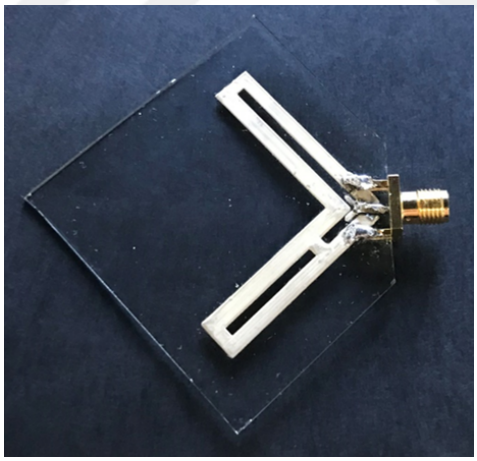

Figure 4.3. The prototype of the optimized model.

4.4. Results and Discussion

Figure 4.4 shows the simulated and measured frequency response of the optimized model for two modes of operation in air. The corresponding center frequency

and the magnitude of the reflection coefficient are tabulated in Table 4.2 along with the corresponding bandwidth values. It can be observed that the simulated frequency responses of the horizontal and vertical mode overlap as expected owing to the symmetry of the design. Moreover, the simulated and measured center frequency agree for the horizontal mode, while the disagreement between the simulated and measured center frequency of the vertical mode is found to be 10 MHz, which can be counted within the limits of manufacturing accuracy. Note that the return loss is greater than 10 dB both for the simulations and the measurements.

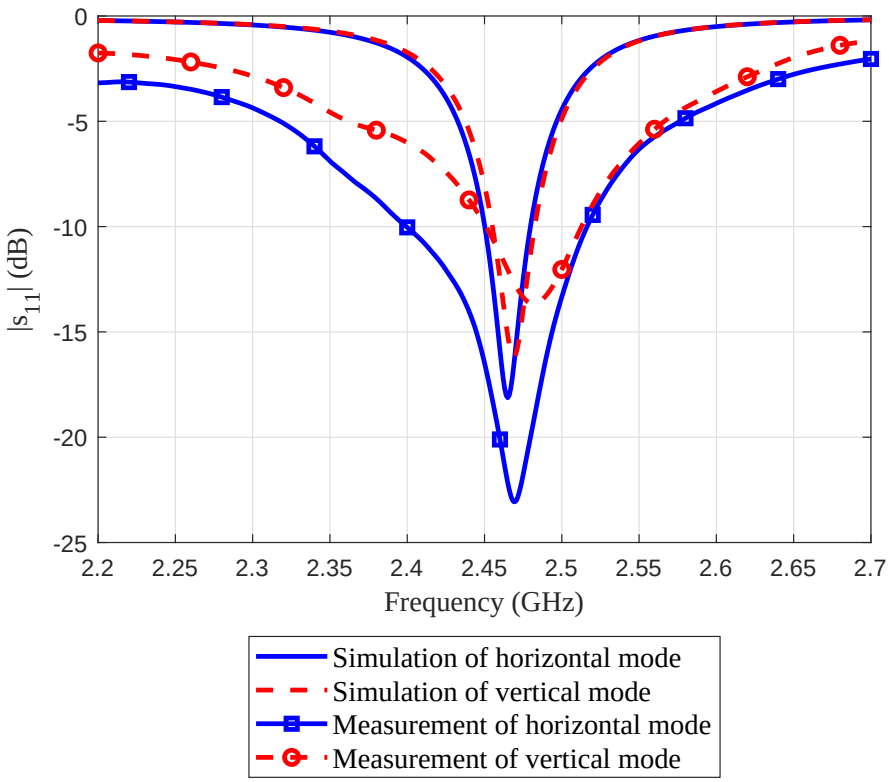

Figure 4.4. Simulated and measured frequency responses of the optimized model in air.

Figure 4.5 shows the simulated 3D radiation patterns at the operating frequency for two modes of operation in air along with the 2D radiation patterns at $\phi = 0°$ and $\phi = 90°$. The position and the value of the maximum gain and the null are tabulated in Table 4.3. It can be seen that in both modes of operation, the patterns are

Table 4.2. The center frequency, the magnitude of the reflection coefficient and the bandwidth for the optimized model in air.

		Center Frequency (GHz)	$\|s_{11}\|$ **(dB)**	**Bandwidth (MHz)**
Horizontal Mode	Simulated	2.47	-18.1	30
	Measured	2.47	-23	120
Vertical Mode	Simulated	2.47	-16.2	20
	Measured	2.48	-13.7	60

bidirectional and have no distortions as expected. Moreover, as in the CBS antenna, the polarizations of the patterns are perpendicular to each other and the position of the null is rotated in the azimuth plane between two modes of operation, which means that the intended polarization and pattern diversity are achieved. The simulated radiation efficiency is determined to be 88% for both modes of operation. The envelope correlation between the two modes, ρ_e, is calculated to be lower than 0.1 using

$$\rho_e = \frac{\left| \int_{4\pi} \int [\vec{F_1}(\theta,\phi) \cdot \vec{F_2}(\theta,\phi)] d\Omega \right|^2}{\int_{4\pi} \int \left| \vec{F_1}(\theta,\phi) \right|^2 d\Omega \int_{4\pi} \int \left| \vec{F_2}(\theta,\phi) \right|^2 d\Omega} \tag{4.4}$$

where $\vec{F_1}(\theta,\phi)$ and $\vec{F_2}(\theta,\phi)$ are the simulated radiation patterns and Ω is the solid angle.

The upper hemisphere of the normalized 3D far-field radiation pattern of the horizontal mode in air is measured using a planar near-field set-up. The measured pattern is shown in Figure 4.6 along with the corresponding 2D cross sections at ϕ = 0° and ϕ = 90°. 2D patterns are plotted considering that the pattern is expected to be symmetrical with respect to xy-plane. It can be noticed that the simulated and measured patterns of the horizontal mode are in good agreement. Using the same planar set-up, the radiation efficiency for the horizontal mode is measured as 41%. However, notice that only the power radiated from the upper hemisphere can

be included in the efficiency measurement due to the operation principle of the planar set-up. Assuming that the pattern is symmetrical with respect to xy-plane, the real efficiency of the horizontal mode can be estimated as 82% (2 × measured efficiency), which is close to the simulated value.

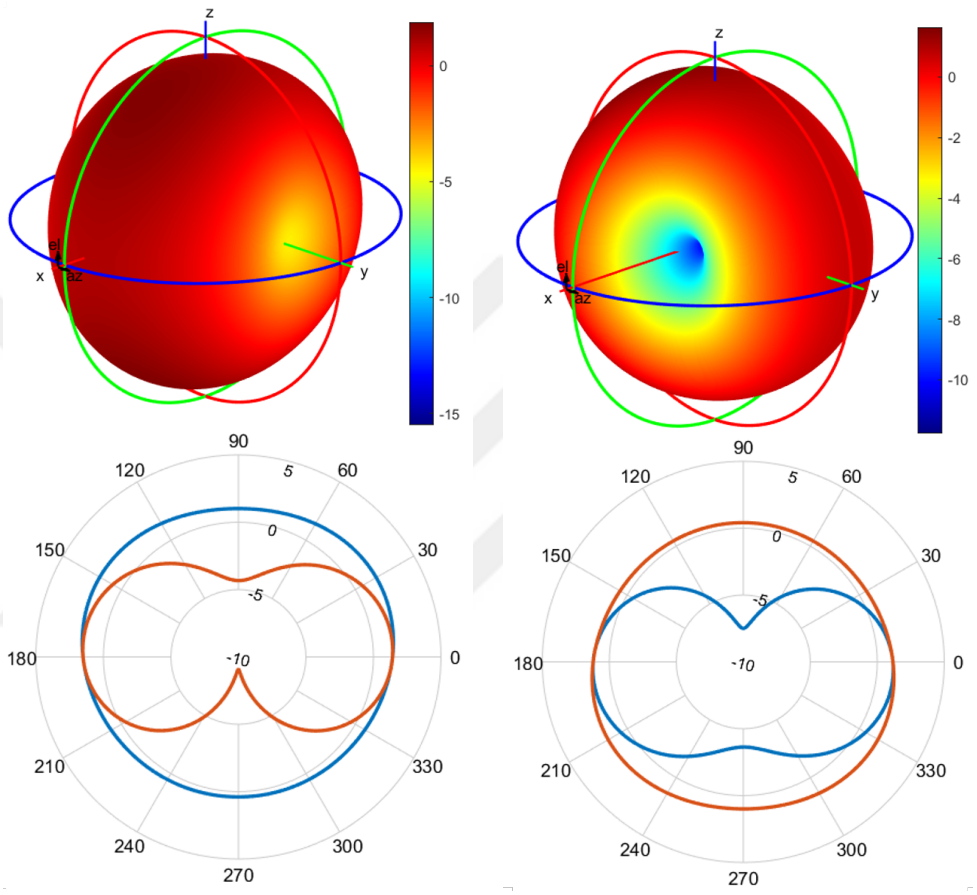

(a) (b)

Figure 4.5. Simulated 3D and 2D radiation patterns (Blue: $\phi = 0°$, Orange: $\phi = 90°$) of the optimized model in air (unit: dBi) (a) the horizontal mode (b) the vertical mode.

Table 4.3. The value and the position of the maximum gain and the null for the optimized model.

		Horizontal Mode	**Vertical Mode**
Maximum Gain	Value (dBi)	1.9	1.6
	Position	$\phi = 8°$ $\theta = 152°$	ϕ = -90° $\theta = 148°$
Null	Value (dBi)	-15.5	-11.8
	Position	ϕ = -106° $\theta = 90°$	$\phi = 18°$ $\theta = 90°$

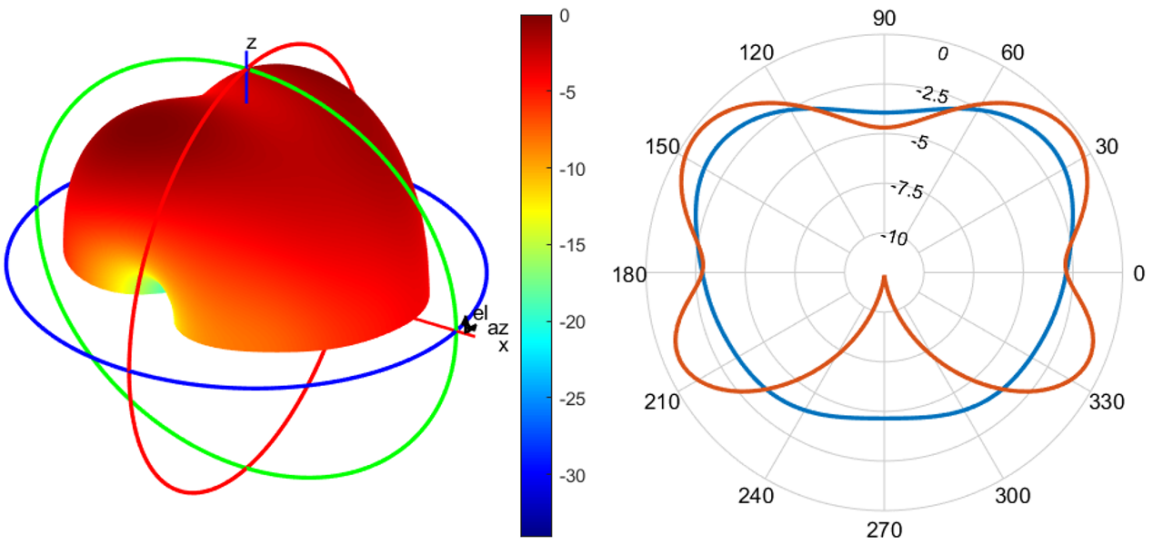

Figure 4.6. Measured normalized 3D and 2D radiation patterns (Blue: $\phi = 0°$, Orange: $\phi = 90°$) of the optimized model in air for the horizontal mode.

5. PIN DIODE IMPLEMENTATION

This chapter presents the realization of the PIN diode circuitry in lieu of the artificial switches as the switching mechanism. The developed PIN diode circuitry and its principle of operation are explained in Section 5.1. The results of the optimized model with PIN diodes in air are presented and discussed in Section 5.2.

5.1. PIN Diode Switching Circuitry

PIN diodes are widely used as high-frequency switches as they have the ability to behave like a resistor with a low resistance when they are forward biased. The forward biasing required to operate the PIN diode as a resistor can be provided by a DC biasing circuitry that however must be isolated from the RF signal path. The resistance of a PIN diode under forward-bias depends on the physical structure of the diode as well as the forward current flowing through it [58]. In order to replace the artificial switches in the optimized model with PIN diodes, the optimized model is slightly modified as shown in Figure 5.1. One 1.2 mm $\times$ 1.2 mm square pad is placed exactly at the switch position determined in Section 4.3 in the horizontal and vertical section of the equilateral L-shaped slot in order to separate the DC bias that will be applied to the PIN diodes from the ground plane of the antenna. The anodes of the PIN diodes (shown in black in Figure 5.1) are connected to these pads, whereas their cathodes (shown in brown in Figure 5.1) are connected to the ground plane of the antenna. NXP BAP 64-03 diodes [59] that have a typical resistance value of 2 Ω under a forward current of 10 mA and a typical forward voltage value of 0.95 V are used as PIN diodes. Similar to the artificial switches, the PIN diodes are biased in an alternating way. A DC bias is applied through a resistor on one of the pads. Therefore, a total resistance of 4 Ω is seen by the RF signal along the two long edges of one of the sections of the slot as shown in Figure 5.1, which can be assumed as a short-circuit. Finally, the optimized model with PIN diodes is prototyped as it is done in the previous models as shown in Figure 5.2.

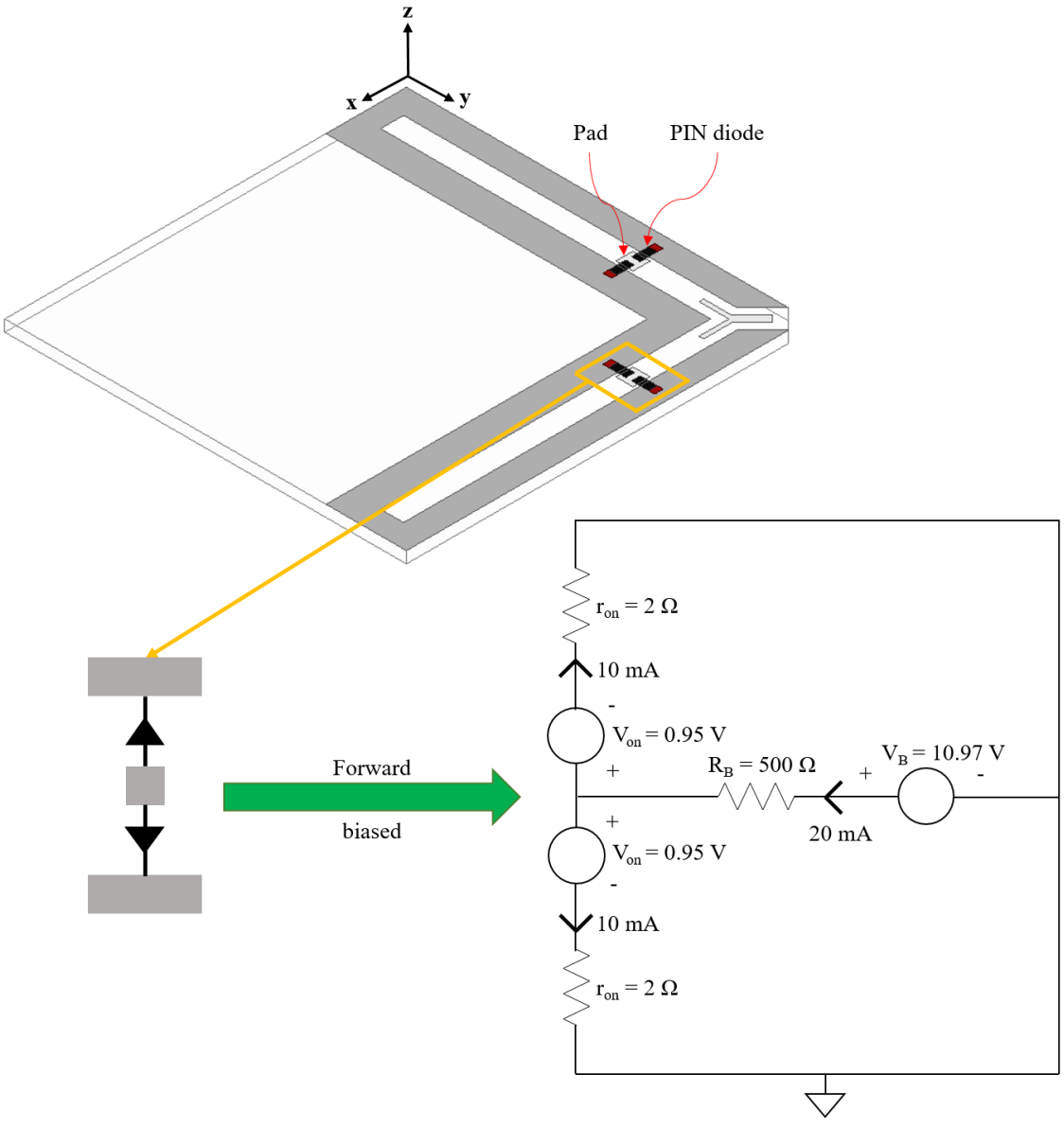

Figure 5.1. The optimized CPW fed slot antenna model with PIN diodes.

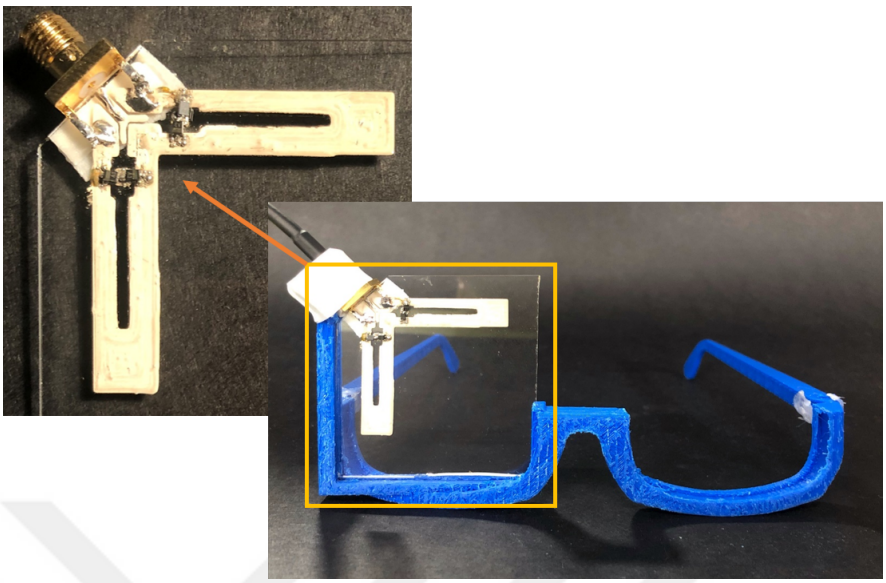

Figure 5.2. The prototype of the optimized model with PIN diodes inserted into a 3D glasses frame.

5.2. Results and Discussion

Figure 5.3 shows the measured frequency response of the optimized model with PIN diodes for two modes of operation in air. The corresponding center frequency and the magnitude of the reflection coefficient are tabulated in Table 5.1. It can be observed that the developed switching circuitry can perform the intended short-circuiting of one of the sections of the slot. However, it can also be seen that compared to the optimized model without PIN diodes, the center frequency for both modes is shifted by 160 MHz with a loss associated with it. The shift in the resonant frequency and the degradation in the matching are predicted to stem from the imperfect shorting provided by the PIN diodes that leads to a greater effective slot length. Therefore, these effects should be taken into account when the model is further to be modified. Nevertheless, as the developed switching circuitry is shown to perform the intended reconfiguration, no further improvements are performed on the model.

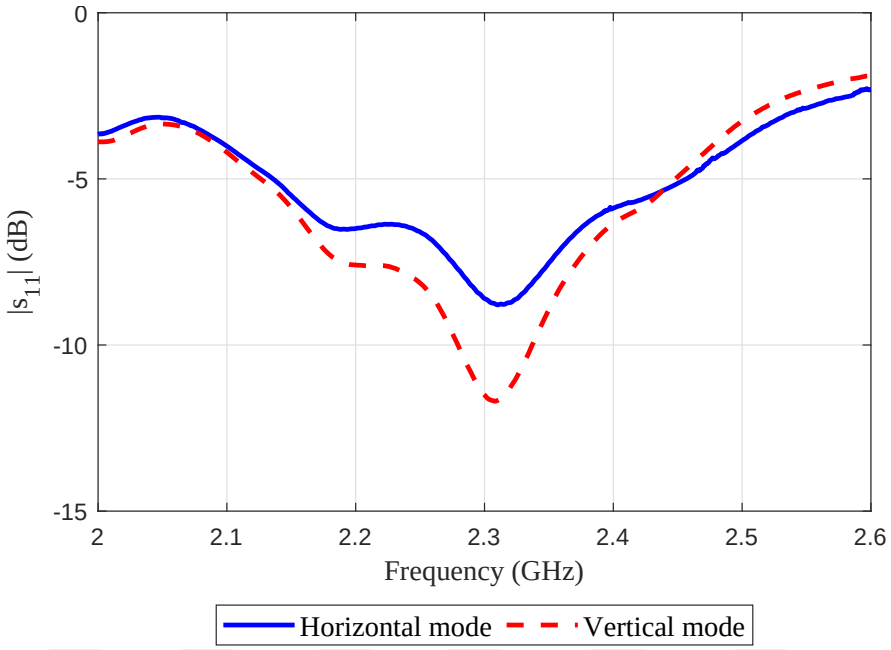

Figure 5.3. Measured frequency responses of the optimized model with PIN diodes in air.

Table 5.1. The center frequency and the magnitude of the reflection coefficient for the optimized model with PIN diodes in air.

	Center Frequency (GHz)	$\|s_{11}\|$ **(dB)**
Horizontal Mode	2.31	-8.77
Vertical Mode	2.31	-11.69

6. ON-BODY PERFORMANCE

As the antenna is intended for the utilization in smart glasses, it will always be operating in close proximity of a human head. As mentioned in Section 2.2, this proximity will lead to detuning effects on the operation of the antenna. Hence, the results in air alone are not sufficient to draw a conclusion on the performance of the antenna and it is essential to determine to what extent the antenna is affected by this proximity. On this purpose, two different measurement set-ups on which the on-body performance of the antenna can be tested are prepared. As will be explained in Section 6.1, phantoms can be used to evaluate these detuning effects. The first measurement set-up is a two-layer phantom that consists of a 3D printed container and two different tissue-mimicking mixtures. Since the eye and the face muscles will be the closest tissues to the antenna when it is used in glasses, the detuning caused by these tissues is likely to be more severe than other types of tissues. Thus, the mixtures used in the two-layer phantom are prepared so that they mimic the electrical properties of the eye tissue and the muscle tissue. The second measurement set-up consists of human subjects wearing the antenna via a 3D printed glasses frame. The numerical versions of the measurement set-ups are prepared as well in order to simulate the effects of the human body and compare the results with the measured ones.

This chapter is organized as follows. Section 6.1 provides the basic knowledge on phantoms. Section 6.2 presents the technique to the fabrication of the tissue-mimicking mixtures used in the two-layer phantom. In Section 6.3, the method used to validate the electrical properties of the mixtures is explained. The completed measurement set-ups and their numerical counterparts are given in Section 6.4. Finally, the on-body results are presented and interpreted in Section 6.5.

6.1. What is a Phantom?

As mentioned previously in Section 2.2, the human body presents a hostile and lossy environment for electromagnetic radiation due to its high electrical properties. Hence, a clear validation of the performance and safety of a device that has electromagnetic interaction with the human body is crucial during the development process [60]. Phantoms are generally chemical formations that can replicate the electrical properties of human tissues [61]. As they can replicate the electrical properties, they are widely used in measurement set-ups developed to accurately evaluate antenna parameter distortions caused by the proximity of the human body [62]. Based on their different features, the phantoms developed to date have been classified in many different ways [63]. For instance, they can be classified in terms of their final forms as solid phantoms [64], semi-solid phantoms [65] or liquid phantoms [66]. Another classification example is the classification in terms of main substance used during the development process that includes water-based phantoms [66], oil-in-gelatine phantoms [67], Triton X100 phantoms [68] and 3D printed phantoms [69]. Finally, phantoms can be grouped based on the part of the body they mimic such as head phantoms [65], hip phantoms [66] or breast phantoms [70].

6.2. Fabrication of Tissue-mimicking Mixtures

The tissue-mimicking mixtures used in the two-layer phantom are water-based, semi-solid mixtures that are prepared using distilled water, cornflour, gelatine, agar, sodium azide, propylene glycol and sodium chloride [65]. The two electrical properties that are replicated by the mixtures are the relative permittivity and the conductivity. The relative permittivity and the conductivity of the eye tissue and the muscle tissue at 2.45 GHz are tabulated in Table 6.1 [71]. The quantity of each ingredient required to prepare the mixtures is provided in Table 6.2.

Table 6.1. Electrical properties of the eye tissue and the muscle tissue at 2.45 GHz.

	Eye Tissue	**Muscle Tissue**
Relative Permittivity	53	52.7
Conductivity (S/m)	2.2	1.74

Table 6.2. The quantity of each ingredient required per 100 g mixture.

	Eye Tissue (g)	**Muscle Tissue (g)**
Distilled Water	75.62	75.62
Cornflour	4.72	4.72
Gelatine	14.53	15.36
Agar	3.02	3.02
Sodium Azide	0.3	0.3
Propylene Glycol	0.6	0.6
Sodium Chloride	1.21	0.38

The procedure to be followed for the fabrication of the mixtures is as follows:

- Step 1: In a beaker, gelatine and agar are added with the two-thirds of distilled water. Tap water is put into a pot and the gelatine-agar mixture is heated gradually to 75°C in the tap water. Heating in tap water must be preferred in lieu of direct heating of the mixture for homogeneous heating. The top of the beaker is covered with aluminium foil to minimize the amount of water evaporating from the beaker. A hole is opened on the aluminium foil and the mixture is continuously stirred with a mixer so that a homogeneous, high-viscosity fluid is obtained.
- Step 2: When the temperature rises to 75°C, sodium chloride is added to the mixture. The temperature is kept constant at 75°C for four minutes.
- Step 3: In another beaker, propylene glycol is added with the rest of the water. Then, cornflour is added by continuously stirring in small portions.
- Step 4: At the end of four minutes, the mixture with cornflour is added to the

other one. The mixture is stirred at 75°C until it becomes homogeneous.

- Step 5: The mixture is allowed to cool at room temperature while it is stirred via a magnetic stirrer. When the temperature drops to 45 °C, sodium azide is added. Cooling is continued until the temperature drops to room temperature.

The given fabrication process is illustrated in Figure 6.1. As water has high permittivity, it is the main source of permittivity in the mixture. Gelatine and agar are used to decrease the permittivity of the mixture. In other words, they are used to control the final permittivity value. Agar has a negligible effect on the permittivity value; however, it helps the thick semi-solid formation of the final mixture. Sodium chloride is the source of conductivity. Propylene glycol is used for stabilizing purposes and sodium azide is used for preservation.

6.3. Measurement of Electrical Properties

Before using the developed tissue-mimicking mixtures in the measurements, it must be validated that the targeted values of electrical properties are reached. In order to measure the electrical properties of the mixtures, the open-ended coaxial probe method is used [72–74].

6.3.1. Theory of the Method

Generally, the permittivity of a homogeneous, linear and isotropic medium is a complex quantity that depends on both the relative permittivity and the conductivity of the medium and given as

$$\epsilon = \epsilon_0(\epsilon_r - j\frac{\sigma}{\omega\epsilon_0}) \tag{6.1}$$

In this method, an open-ended coaxial cable which is immersed into the test medium is used as the probe. The fringing electric fields inside the test medium at the extremity of the cable are modeled using a virtual transmission line length; that is, the coaxial

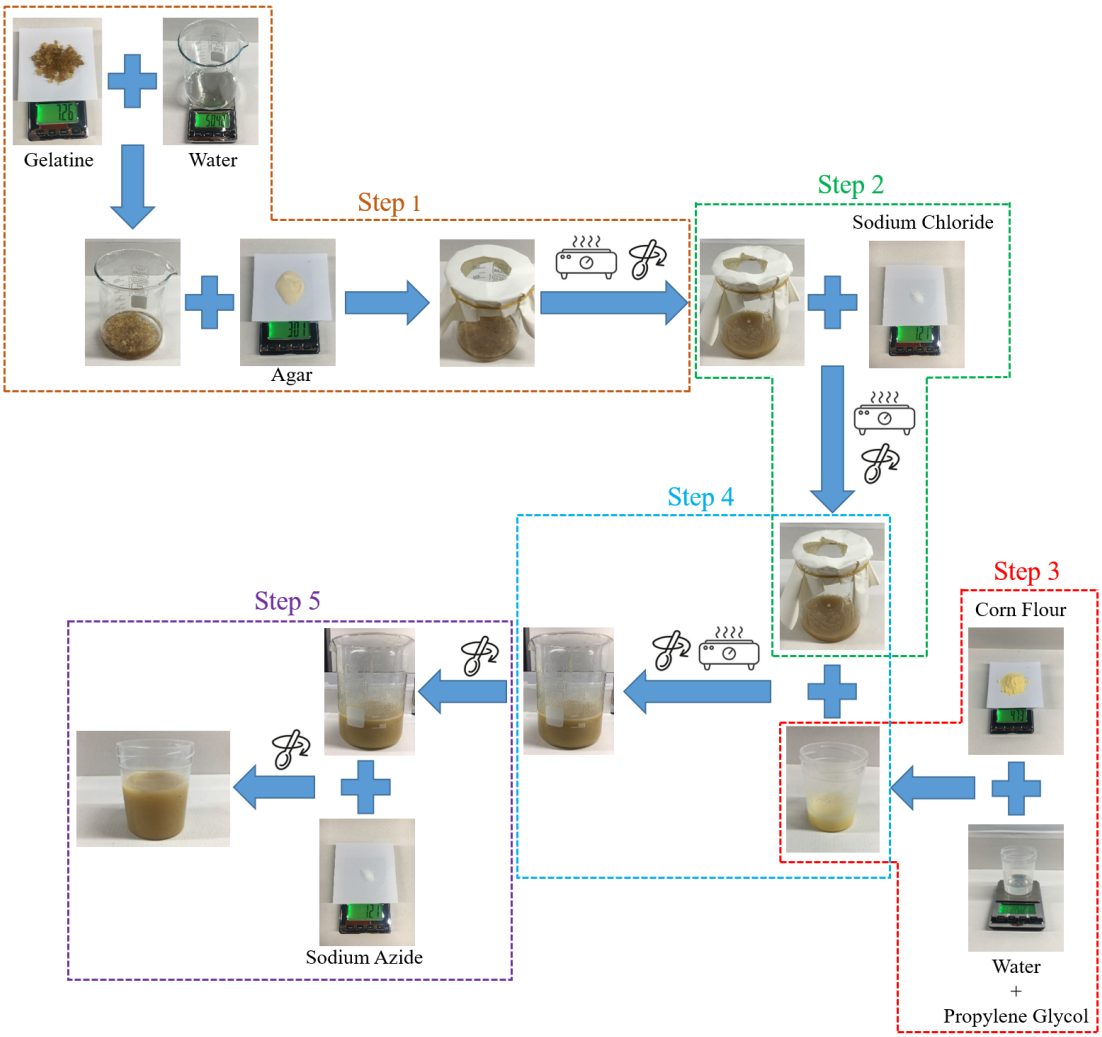

Figure 6.1. The procedure to be followed to develop the tissue-mimicking mixtures.

cable is assumed to extend inside the test medium as visualized in Figure 6.2. The permittivity of the test medium is determined by relating it to the measured reflection coefficient. Note that the relative permittivity of the test medium is taken as the relative permittivity of the virtual transmission line.

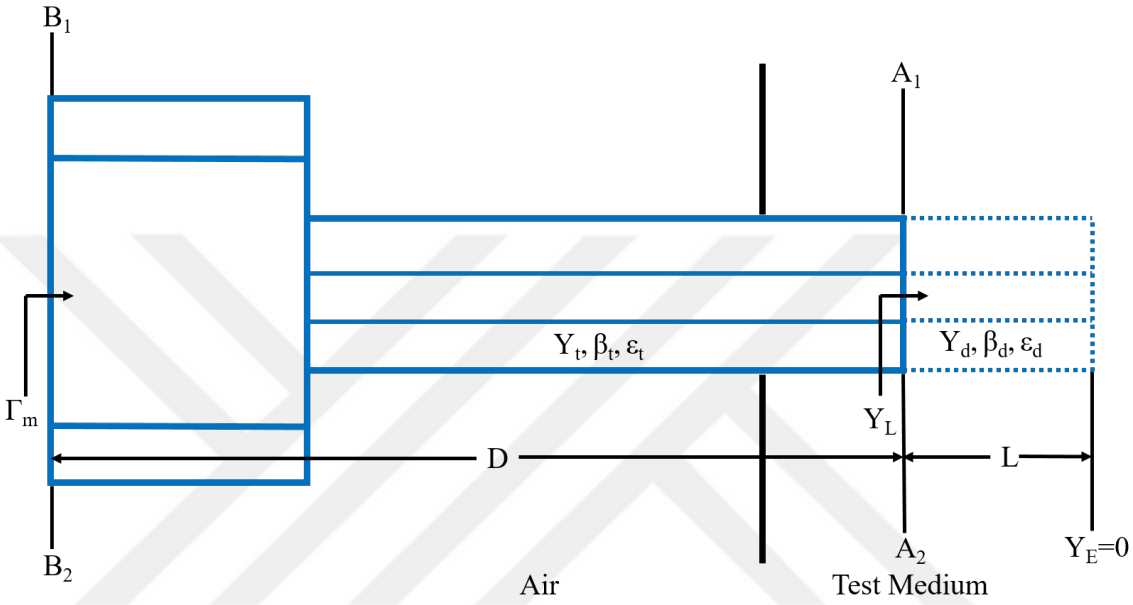

Figure 6.2. The open-ended coaxial probe model.

The variables included in Figure 6.2 are listed as follows:

- Y_L: The admittance at the input of the virtual transmission line
- Y_E: Terminating admittance at the end of the virtual transmission line
- Y_t: Characteristic admittance of the probe
- β_t: Propagation constant in the probe
- ϵ_t: Complex permittivity of the material used in the probe
- Y_d: Characteristic admittance of the virtual transmission line
- β_d: Propagation constant in the test medium
- ϵ_d: Complex permittivity of the test medium
- D: Physical length of the probe

- L: Virtual transmission line length
- Γ_m: Reflection coefficient measured at plane B_1B_2

If a quasi-TEM mode is assumed for the wave propagating in the coaxial cable, the complex admittance at plane A_1A_2 can be given as

$$Y_L = Y_d \frac{Y_E + jY_d tan(\beta_d L)}{Y_d + jY_E tan(\beta_d L)} \tag{6.2}$$

As the radiation losses can be neglected, the terminating impedance can be considered as a fully-reflecting open circuit (Y_E=0) and Equation 6.2 simplifies to

$$Y_L = jY_d tan(\beta_d L) \tag{6.3}$$

The characteristic admittance of a lossless transmission line is given as

$$Y_0 = \sqrt{\frac{C}{L}} \tag{6.4}$$

where C is the capacitance and L is the inductance of the line. For coaxial cables, the capacitance and the inductance are expressed as

$$C = \frac{2\pi\epsilon}{ln(b/a)} \tag{6.5}$$

$$L = \frac{\mu}{2\pi} ln(b/a) \tag{6.6}$$

where a and b are the inner and the outer radii of the coaxial cable, respectively. Substituting Equation 6.5 and Equation 6.6 into Equation 6.4, Y_d and Y_t can be expressed as

$$Y_d = \frac{\sqrt{\epsilon_d}}{60 ln(b/a)} \tag{6.7}$$

$$Y_t = \frac{\sqrt{\epsilon_t}}{60ln(b/a)} \tag{6.8}$$

Moreover, the admittance Y_L can be expressed in terms of the characteristic admittance of the probe Y_t and the reflection coefficient measured at plane B_1B_2 as

$$Y_L = \left[\frac{1-\Gamma_m e^{2j\beta_t D}}{1+\Gamma_m e^{2j\beta_t D}}\right] Y_t \tag{6.9}$$

By substituting Equation 6.3, Equation 6.7 and Equation 6.8 into Equation 6.9, one can obtain

$$j\frac{\sqrt{\epsilon_d}}{60ln(b/a)} tan(\beta_d L) = \left[\frac{1-\Gamma_m e^{2j\beta_t D}}{1+\Gamma_m e^{2j\beta_t D}}\right] \frac{\sqrt{\epsilon_t}}{60ln(b/a)} \tag{6.10}$$

The propagation constant in the test medium β_d can be expressed as

$$\beta_d = w\sqrt{LC} = 2\pi f\sqrt{\epsilon\mu} = 2\pi f\sqrt{\epsilon_0\mu_0\epsilon_d} = \frac{2\pi f\sqrt{\epsilon_d}}{c} \tag{6.11}$$

By substituting Equation 6.11 into Equation 6.10, one can get

$$\sqrt{\epsilon_d} = -j\sqrt{\epsilon_t}\left[\frac{1-\Gamma_m e^{2j\beta_t D}}{1+\Gamma_m e^{2j\beta_t D}}\right] cot\left(\frac{2\pi f L\sqrt{\epsilon_d}}{c}\right) \tag{6.12}$$

which is rearranged to have

$$\epsilon_d = \left[\frac{-jc\sqrt{\epsilon_t}}{2\pi f L}\right]\left[\frac{1-\Gamma_m e^{2j\beta_t D}}{1+\Gamma_m e^{2j\beta_t D}}\right]\left[\frac{2\pi f L\sqrt{\epsilon_d}}{c}\right] cot\left(\frac{2\pi f L\sqrt{\epsilon_d}}{c}\right) \tag{6.13}$$

Equation 6.13 is the final equation that will be used in order to compute the complex permittivity of the test medium from the measured reflection coefficient. Note that the two probe parameters, D and L, must be determined at the operating frequency. These parameters are determined by using two reference dielectric mediums of which permittivities are known. The reflection coefficients when the probe is immersed into

the reference mediums are measured and D and L are calculated iteratively by using the measured reflection coefficients and the permittivities of the reference mediums. The procedure for the iteration process is summarized in [72]. In this work, air ($\epsilon_r = 1$) and deionized water ($\epsilon_r = 80$) are selected as reference mediums for their simplicity. A MATLAB code implementing the iteration process is developed for the complex calculations.

6.3.2. Experimental Studies and Measurements

The implemented model can be validated experimentally by measuring a sample medium of which permittivity is already known. For this purpose, ethanol is used as the sample medium and the determined permittivity values are compared with the ones in the literature [75]. A 9 cm RG402 semi-rigid coaxial cable is used as the probe and the measurements in the reference mediums are taken as shown in Figure 6.3. The reflection coefficients are measured using PICO VNA106 which is calibrated in 2-4 GHz frequency band. The computed relative permittivity and the dielectric loss factor of

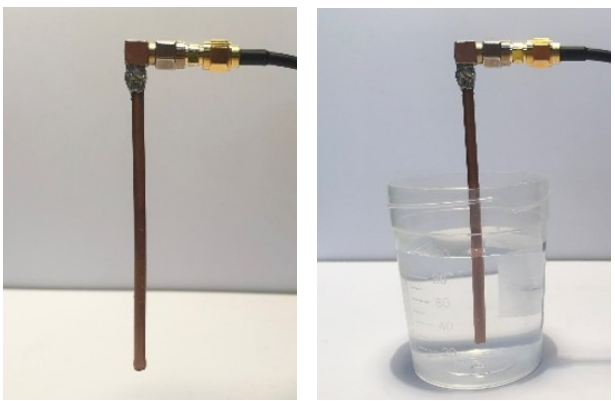

(a) (b)

Figure 6.3. Measurements taken in the reference mediums (a) air (b) deionized water.

ethanol are shown in Figure 6.4. The conductivity can be calculated from the dielectric loss factor using

$$\sigma = \epsilon_r'' \omega \epsilon_0 \tag{6.14}$$

where ϵ_r'' is the dielectric loss factor. It is observed that the computed values are in good agreement with the literature. Hence, it can be concluded that the model functions as expected and can be used to measure the electrical properties of the mixtures.

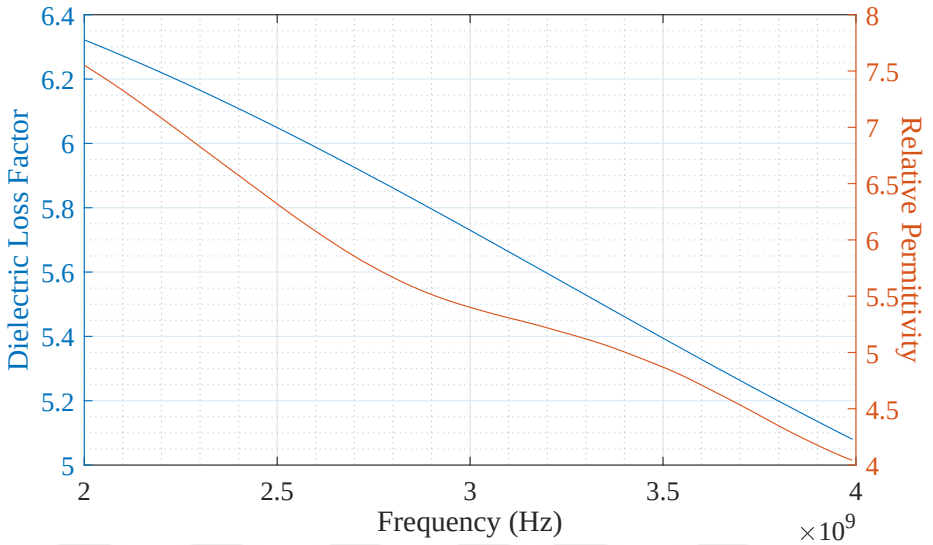

Figure 6.4. The computed dielectric loss factor and relative permittivity of ethanol.

The computed relative permittivity and the conductivity of the tissue-mimicking mixtures at 2.45 GHz are tabulated in Table 6.3 along with the real values. The disagreement between the real and computed values is predicted to be caused by the evaporation of water throughout the fabrication. This disagreement can be presented as percent error. As can be seen in Table 6.3, the percent error for each case is less than 15%. Thus, the disagreement can be counted within the limits of manufacturing accuracy.

6.4. Completed Measurement Set-ups

In order to build up a two-layer phantom from the developed mixtures, a 10 cm × 10 cm × 10 cm container is designed for 3D printing as shown in Figure 6.5. A special compartment for the eye phantom is located in the center of the container

Table 6.3. Computed electrical properties of the two tissue-mimicking mixtures and the real values at 2.45 GHz.

		Eye Tissue	**Muscle Tissue**
Relative Permittivity	Real Value	53	52.7
	Computed Value	48	48.5
	Percent Error	9.4%	8%
Conductivity (S/m)	Real Value	2.2	1.74
	Computed Value	2.5	2
	Percent Error	13.6%	14.9%

and a planar clamp is placed at one of the corners to fix the antenna and the cabling during the measurements. The 3D printed container is made of PLA and covered with waterproof spray so that no leakage occurs. A circular latex balloon is filled with the eye-mimicking mixture and placed at its special compartment. The container is then filled with the muscle-mimicking mixture and the antenna is placed at the planar clamp. The finalized two-layer phantom can be seen in Figure 6.6(b). For the measurements on human subjects, the antenna is worn by human subjects via a 3D printed glasses frame as seen in Figure 6.6(c). The corresponding simulations are run on ANSYS human body phantom, Male-4 mm accuracy as shown in Figure 6.6(d).

6.5. On-body Results and Discussion

Figure 6.7 shows the simulated and measured frequency response of the optimized model for two modes of operation on the two-layer phantom along with the simulated frequency responses on ANSYS human body phantom. The corresponding center frequency and the magnitude of the reflection coefficient are tabulated in Table 6.4. It can be noticed that the antenna operates in the desired band with a return loss greater than 10 dB for all different cases. It can also be seen from Figure 6.7 that the simulated center frequencies on the two-layer phantom are lower than the measured ones. This difference is predicted to result from the inaccuracies in the physical and electrical

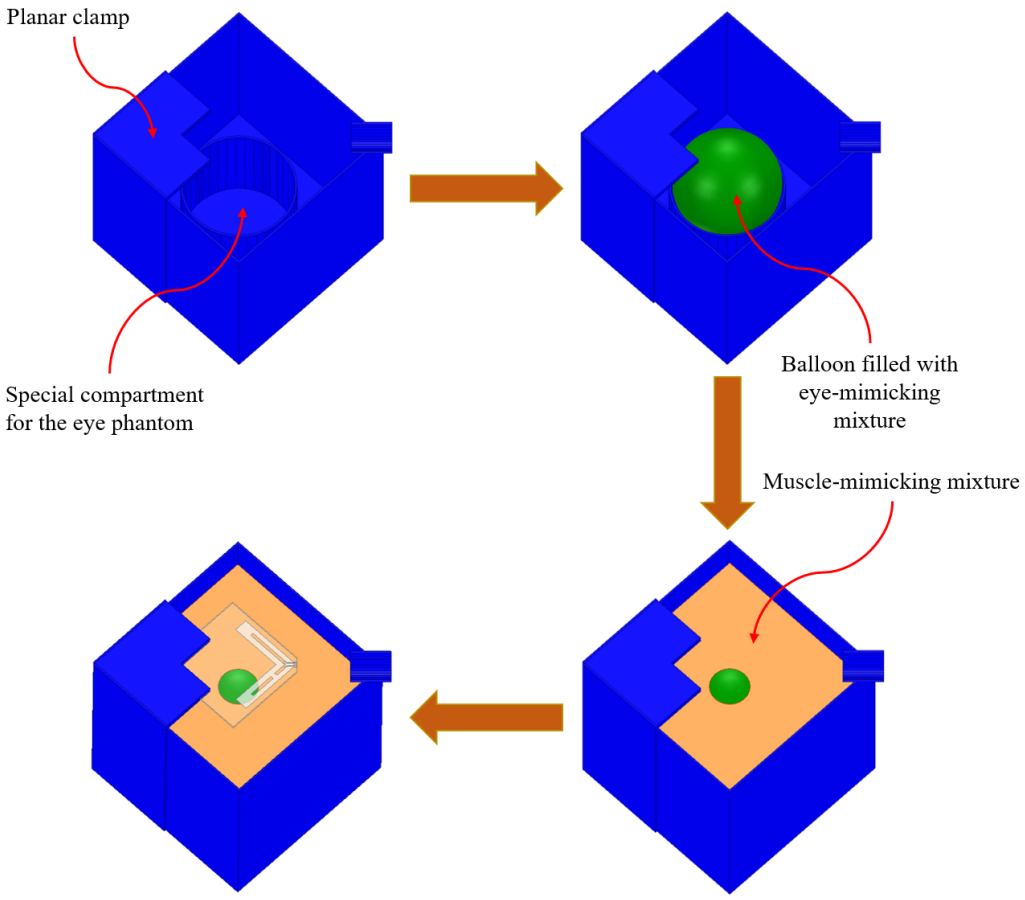

Figure 6.5. The steps to prepare the two-layer phantom.

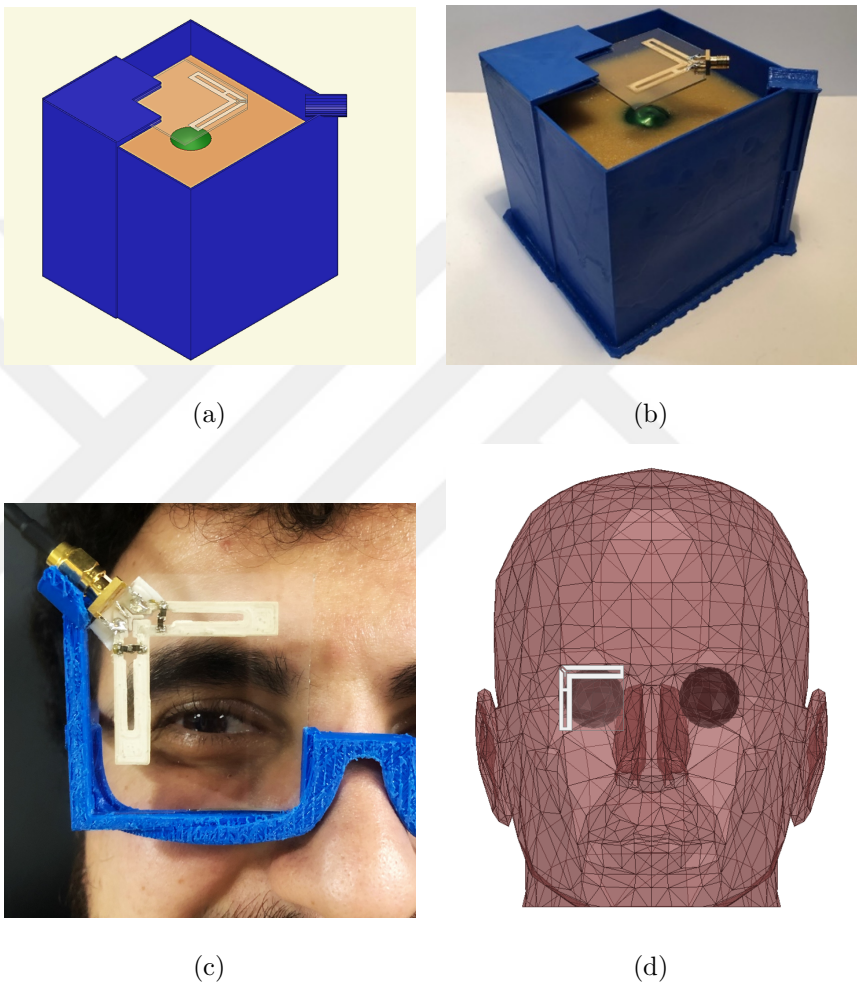

(a) (b)

(c) (d)

Figure 6.6. Set-ups used to evaluate the on-body performance of the antenna and their numerical counterparts (a) numeric two-layer phantom (b) physical two-layer phantom (c) the antenna worn by a human (d) ANSYS human body phantom.

properties of the tissue-mimicking mixtures used in the simulations. Another important point that can be observed in Figure 6.7 is that the simulated center frequencies on the two-layer phantom and on ANSYS human body phantom differ from each other. The reason behind this is estimated to be the simplicity of the two-layer phantom. This result indicates that final measurements are required to be taken on human subjects in order to draw a more reliable conclusion on the on-body performance of the antenna.

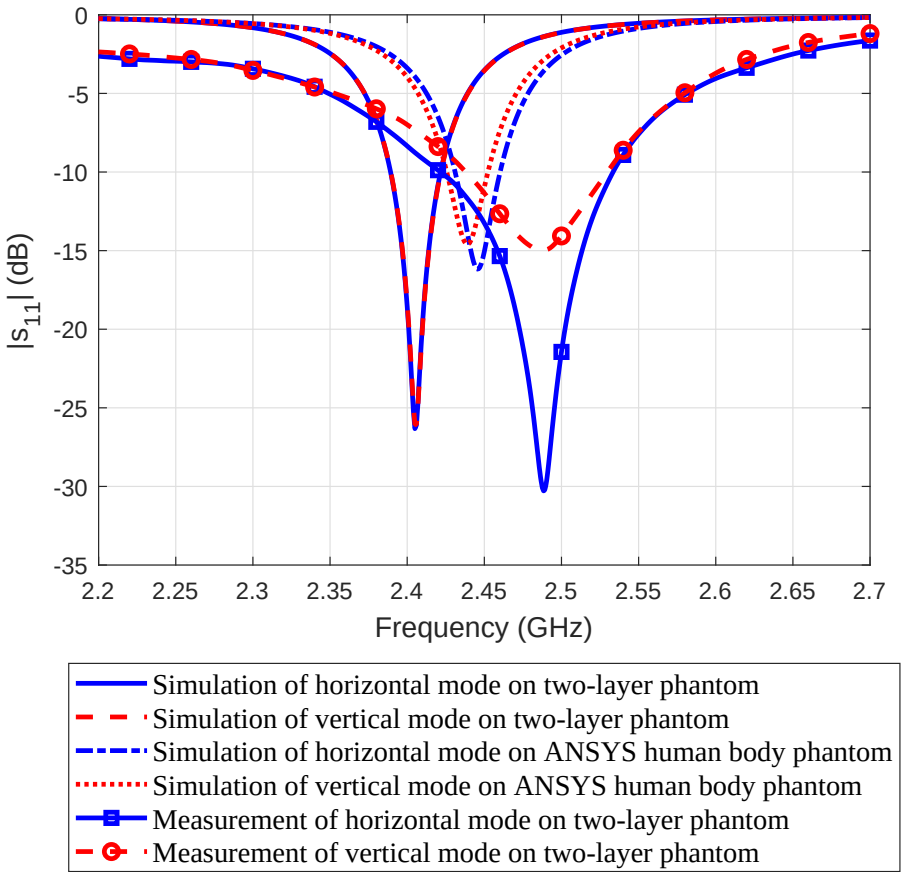

Figure 6.7. Simulated and measured frequency responses of the optimized model on the two-layer phantom and on ANSYS human body phantom.

Figure 6.8 shows the measured frequency response of the optimized model with both the artificial switches and PIN diodes for two modes of operation on human subjects. The mean and the standard deviation of the corresponding center frequency

Table 6.4. The center frequency and the magnitude of the reflection coefficient for the optimized model on the two-layer phantom and on ANSYS human body phantom.

			Center Frequency (GHz)	$\|s_{11}\|$ **(dB)**
Two-layer Phantom	**Horizontal Mode**	Simulated	2.41	-26.1
		Measured	2.49	-30.3
	Vertical Mode	Simulated	2.41	-26.3
		Measured	2.49	-15
ANSYS Human Body Phantom	**Horizontal Mode**		2.44	-16
	Vertical Mode		2.44	-14.4

and magnitude of the reflection coefficient are tabulated in Table 6.5. It can be seen that the center frequencies given in Figure 6.8 are in good agreement with the center frequencies that are measured in air and presented in Figure 4.4 and Figure 5.3, while there is a loss in the return loss for each case as expected due to the effect of the human body. Nevertheless, the return loss with a mean of 8.35 dB for different cases is found to be reasonable for the operation near the human body. Furthermore, the center frequency does not change for different subjects, whereas the magnitude of the reflection coefficient changes in the order of 1 dB. These results support the initial assumption that owing to their magnetic nature, slot antennas are more robust to detuning effects and hence more suitable for the operation near the human body.

Figure 6.9 shows the simulated 3D radiation patterns at the operating frequency for two modes of operation on ANSYS human body phantom along with the 2D radiation patterns at $\phi = 0°$ and $\phi = 90°$. It can be noticed that the pattern of both modes has become directional due to the effect of the phantom. The maximum gain is determined to be 2.3 dBi for the horizontal mode and 4.3 dBi for the vertical mode. The simulated radiation efficiency is found to be 41% for the horizontal mode and 56% for the vertical mode, whereas it was 88% for both modes of operation in air as mentioned in Section 4.4. The degradation in the radiation efficiency when operating near

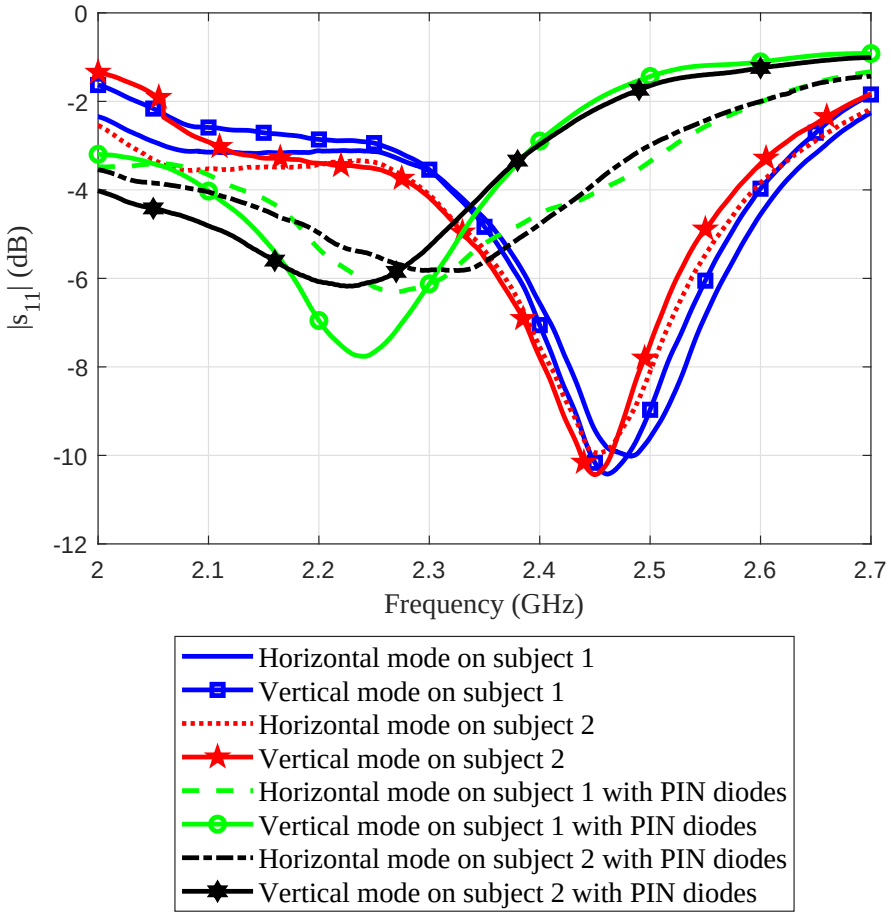

Figure 6.8. Measured frequency responses of the optimized model with both the artificial switches and PIN diodes on human subjects.

Table 6.5. The mean and the standard deviation of the center frequency and the magnitude of the reflection coefficient measured on human subjects.

	Mean	**Standard Deviation**
Center Frequency	2.36 GHz	0.1 GHz
$\|\mathbf{s}_{11}\|$	-8.35 dB	1.92 dB

the human body is expected due to the bulk power absorption by the body. However, the fact that the horizontal mode has a lower on-body radiation efficiency than the vertical mode indicates that the horizontal mode couples more to the human body.

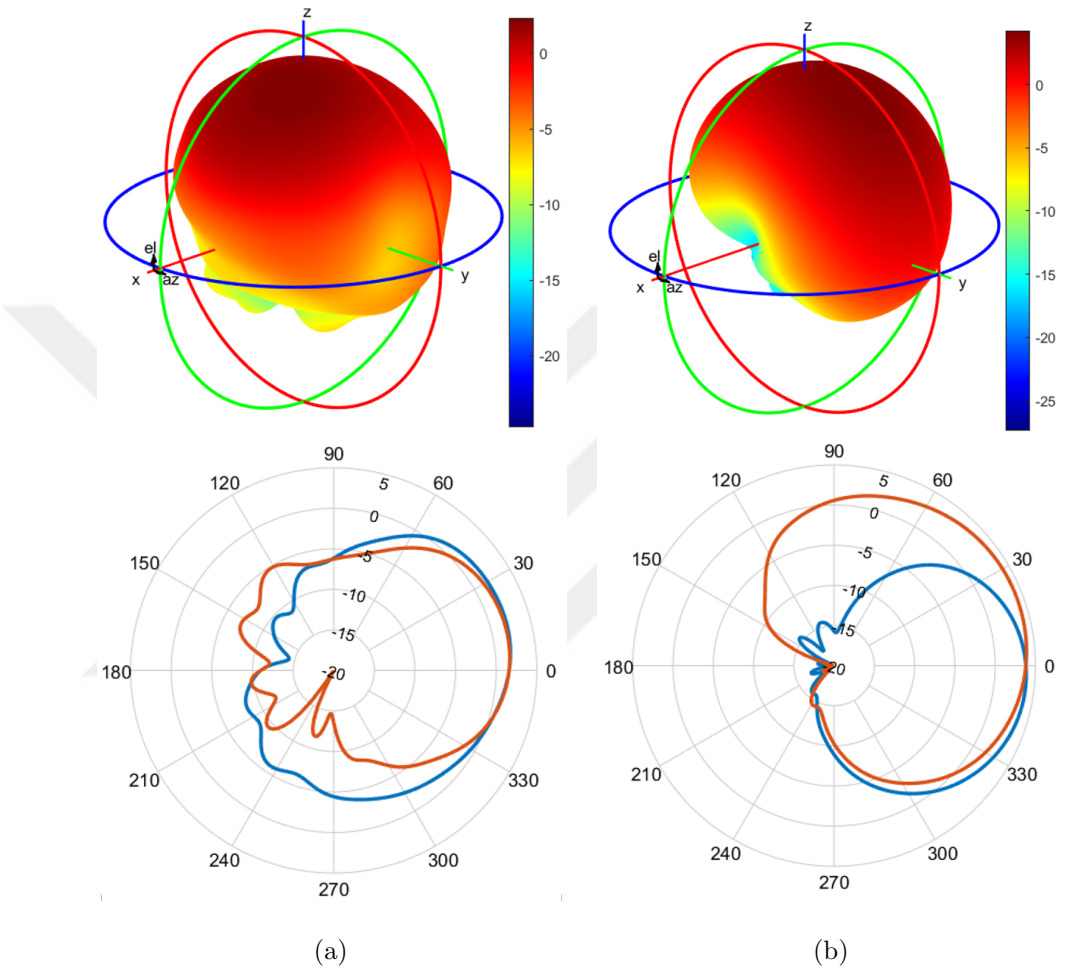

(a) (b)

Figure 6.9. Simulated 3D and 2D radiation patterns (Blue: $\phi = 0°$, Orange: $\phi = 90°$) of the optimized model on ANSYS human body phantom (unit: dBi) (a) the horizontal mode (b) the vertical mode.

Figure 6.10 shows the simulated Specific Absorption Rate (SAR) of the optimized model at the operating frequency for two modes of operation. The SAR is a measure of the energy absorbed per unit mass by a human body when it has an interaction with an RF electromagnetic field. In the European Standards, the limit of SAR for safe exposure to an RF electromagnetic energy is specified as 2 W/kg. As can be

seen in Figure 6.10, the maximum SAR is determined to be less than 0.95 W/kg for the horizontal mode and 0.8 W/kg for the vertical mode, which indicates that both values are well below the specified limit. Notice that the maximum SAR value for the horizontal mode is greater than the one for the vertical mode, which supports the argument that the horizontal mode couples more to the human body.

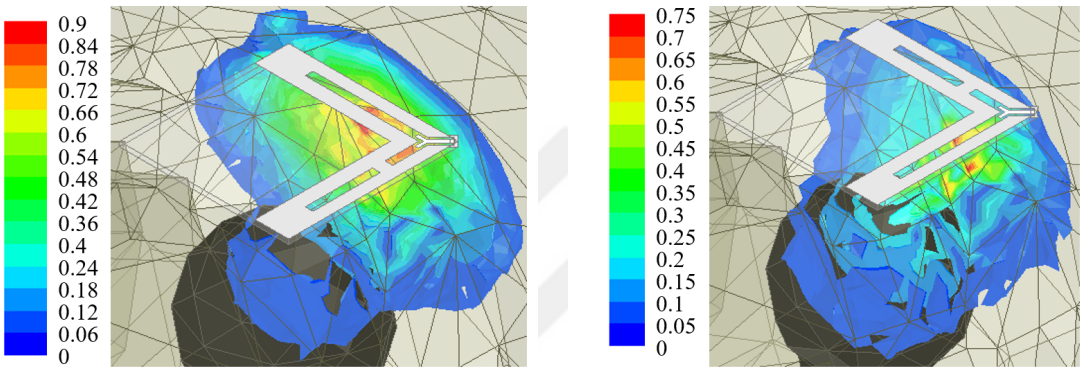

(a) (b)

Figure 6.10. Simulated SAR of the optimized model for two modes of operation (unit: W/kg) (a) the horizontal mode (b) the vertical mode.

7. CONCLUSION

Reconfigurable antennas are widely implemented in wearable devices as they can ensure that the quality of the wireless link formed by these devices is kept above the desired level while the surrounding environmental conditions alter. In this work, a novel pattern and polarization reconfigurable wearable slot antenna that is suitable for the utilization in smart glasses is proposed. The antenna operates in the 2.4 GHz ISM band and consists of an equilateral L-shaped slot that is fed by a single CPW feed. Glass is used as the substrate of the antenna. The antenna is switched between two modes of operation that are generated by manipulating the slot via switches. Two states of switches lead to two L-shaped slots that are aligned in different directions. Therefore, the patterns created by the L-shaped slots are polarized in perpendicular to each other and have their nulls in different positions. The switching between the modes is initially achieved using artificial switches. Afterwards, the artificial switches are replaced by a switching mechanism consisting of 4 PIN diodes that are biased externally. The analytical design, the numerical optimization and the fabrication process of the proposed antenna are explained in detail along with the two preliminary models that form the basis of the approach used to design the proposed antenna. As it is a wearable antenna, measurement set-ups consisting of a two layer-phantom and human subjects are prepared to evaluate the on-body performance of the antenna. The simulation and measurement results in air and on the prepared measurement set-ups are given and interpreted. According to the results, the antenna is shown to perform well in air as well as near the human body with a calculated correlation between the two modes less than 0.1, a maximum gain greater than 1.5 dBi and efficiency greater than 40% in all different cases. Finally, the SAR values are shown to be below the limit specified in the European Standards through simulations. The model may further be optimized in order to increase its bandwidth such that it covers the whole 2.4 GHz ISM band in all cases. Another further optimization can be performed on the optimized model with PIN diodes such that it operates approximately at 2.45 GHz with a better return loss. In addition, if the external biasing circuitry can in some way be implemented on the

glass along with the antenna, the design can be turned into a more robust design.

The proposed model is determined to be promising for wearable applications. However, even though the optimized model is shown to operate as desired as a single element, its performance in a complete communication system is yet to be determined. Thus in the future work, system-level tests can be performed to increase the reliability of the antenna. The effect of using the reconfigurable antenna on the power levels received by the access point can be evaluated by a realistic set-up such as an in-house scenario. In the realistic set-up, the selection between the two modes can be performed according to the power of the received signal at each mode. In the case of an unreliable link when operating in one of the modes, the selection must be activated as soon as possible in order to minimize the power loss resulting from RF retransmissions. For this purpose, a threshold for the received signal can be determined below which the selection will be activated. According to the results of system-level tests, the model can be modified if necessary.

REFERENCES

1. Fantana, N., T. Riedel, J. Schlick, S. Ferber, J. Hupp, S. Miles, F. Michahelles and S. Svensson, *Internet of Things - Converging Technologies for Smart Environments and Integrated Ecosystems*, pp. 153–204, River Publishers, 2013.

2. Islam, S. M. R., D. Kwak, M. H. Kabir, M. Hossain and K. Kwak, "The Internet of Things for Health Care: A Comprehensive Survey", *IEEE Access*, Vol. 3, pp. 678–708, 2015.

3. Vasanth, K. and J. Sbert, *Creating Solutions for Health through Technology Innovation (Texas Instruments)*, 2016, `https://www.ti.com/lit/wp/sszy006/sszy006.pdf`, accessed at July 2020.

4. El Abbasi, M. and K. Kabalan, "Revolutionizing the Development of Wearable Antennas", *International Workshop on Antenna Technology (iWAT)*, pp. 54–57, 2019.

5. Shah, S. A., D. Fan, Z. Zhang, N. Zhao, X. Yang, M. Luo, W. Wang, F. Hu, M. Ur Rehman, O. Badarneh and Q. Abbasi, "Internet of Things for Sensing: A Case Study in the Healthcare System", *Applied Sciences*, Vol. 8, pp. 508–524, 2018.

6. Tobón, D. P., T. H. Falk and M. Maier, "Context Awareness in WBANs: A Survey on Medical and Non-Medical Applications", *IEEE Wireless Communications*, Vol. 20, No. 4, pp. 30–37, 2013.

7. Paracha, K. N., S. K. Abdul Rahim, P. J. Soh and M. Khalily, "Wearable Antennas: A Review of Materials, Structures, and Innovative Features for Autonomous Communication and Sensing", *IEEE Access*, Vol. 7, pp. 56694–56712, 2019.

8. Balanis, C. A., *Antenna Theory: Analysis and Design*, John Wiley & Sons, 2016.

9. Kraus, J. D. and R. J. Marhefka, *Antennas for All Applications*, McGraw-Hill, 2002.

10. Milligan, T. A., *Modern Antenna Design*, John Wiley & Sons, 2005.

11. Stutzman, W. L. and G. A. Thiele, *Antenna Theory and Design*, John Wiley & Sons, 2012.

12. Chen, W. K., *The Electrical Engineering Handbook*, Elsevier, 2005.

13. Abbas, S. M., K. P. Esselle, L. Matekovits, M. Rizwan and L. Ukkonen, "On-Body Antennas: Design Considerations and Challenges", *URSI International Symposium on Electromagnetic Theory (EMTS)*, pp. 109–110, 2016.

14. Dumanli, S., "Challenges of Wearable Antenna Design", *46th European Microwave Conference (EuMC)*, pp. 1350–1352, 2016.

15. Ma, S., L. Ukkonen, L. Sydänheimo and T. Björninen, "Comparison of Human Head Phantoms with Different Complexities for Implantable Antenna Development", *International Applied Computational Electromagnetics Society Symposium - China (ACES)*, pp. 1–2, 2018.

16. Skrivervik, A. K., M. Bosiljevac, J. Trajkovikj, B. Fuchs and Z. Sipus, "Design Considerations for Wearable Antennas", *URSI International Symposium on Electromagnetic Theory (EMTS)*, pp. 524–527, 2016.

17. Conway, G. A. and W. G. Scanlon, "Antennas for Over-Body-Surface Communication at 2.45 GHz", *IEEE Transactions on Antennas and Propagation*, Vol. 57, No. 4, pp. 844–855, 2009.

18. Scanlon, W. G. and N. E. Evans, "Numerical Analysis of Bodyworn UHF Antenna Systems", *Electronics Communication Engineering Journal*, Vol. 13, No. 2, pp. 53–64, 2001.

19. Hall, P. S., Y. Hao, Y. I. Nechayev, A. Alomainy, C. C. Constantinou, C. Parini, M. R. Kamarudin, T. Z. Salim, D. T. M. Hee, R. Dubrovka, A. S. Owadally, W. Song, A. Serra, P. Nepa, M. Gallo and M. Bozzetti, "Antennas and Propagation for On-Body Communication Systems", *IEEE Antennas and Propagation Magazine*, Vol. 49, No. 3, pp. 41–58, 2007.

20. Dumanli, S., "On-Body Antenna with Reconfigurable Radiation Pattern", *IEEE MTT-S International Microwave Workshop Series on RF and Wireless Technologies for Biomedical and Healthcare Applications (IMWS-Bio2014)*, pp. 1–3, 2014.

21. Costantine, J., Y. Tawk, S. E. Barbin and C. G. Christodoulou, "Reconfigurable Antennas: Design and Applications", *Proceedings of the IEEE*, Vol. 103, No. 3, pp. 424–437, 2015.

22. Christodoulou, C. G., Y. Tawk, S. A. Lane and S. R. Erwin, "Reconfigurable Antennas for Wireless and Space Applications", *Proceedings of the IEEE*, Vol. 100, No. 7, pp. 2250–2261, 2012.

23. Chen, S. J., D. C. Ranasinghe and C. Fumeaux, "A Robust Snap-On Button Solution for Reconfigurable Wearable Textile Antennas", *IEEE Transactions on Antennas and Propagation*, Vol. 66, No. 9, pp. 4541–4551, 2018.

24. Dubal, S. and A. Chaudhari, "Mechanisms of Reconfigurable Antenna: A Review", *10th International Conference on Cloud Computing, Data Science Engineering (Confluence)*, pp. 576–580, 2020.

25. Salleh, S. M., M. Jusoh, A. H. Ismail, M. R. Kamarudin, P. Nobles, M. K. A. Rahim, T. Sabapathy, M. N. Osman, M. I. Jais and P. J. Soh, "Textile Antenna with Simultaneous Frequency and Polarization Reconfiguration for WBAN", *IEEE Access*, Vol. 6, pp. 7350–7358, 2018.

26. Saeed, S. M., C. A. Balanis, C. R. Birtcher, A. C. Durgun and H. N. Shaman,

"Wearable Flexible Reconfigurable Antenna Integrated with Artificial Magnetic Conductor", *IEEE Antennas and Wireless Propagation Letters*, Vol. 16, pp. 2396–2399, 2017.

27. Singh, A., I. Goode and C. E. Saavedra, "A Multistate Frequency Reconfigurable Monopole Antenna Using Fluidic Channels", *IEEE Antennas and Wireless Propagation Letters*, Vol. 18, No. 5, pp. 856–860, 2019.

28. Simorangkir, R. B. V. B., Y. Yang, K. P. Esselle and Y. Diao, "A Varactor-Tuned Frequency-Reconfigurable Fabric Antenna Embedded in Polymer: Assessment of Suitability for Wearable Applications", *IEEE MTT-S International Microwave Symposium (IMS)*, pp. 204–207, 2017.

29. Jilani, S. F., B. Greinke, Yang Hao and A. Alomainy, "Flexible Millimetre-Wave Frequency Reconfigurable Antenna for Wearable Applications in 5G Networks", *URSI International Symposium on Electromagnetic Theory (EMTS)*, pp. 846–848, 2016.

30. Jilani, S. F. and A. Alomainy, "An Inkjet-Printed MMW Frequency-Reconfigurable Antenna on a Flexible PET Substrate for 5G Wireless Systems", *Loughborough Antennas Propagation Conference (LAPC)*, pp. 1–3, 2017.

31. Lee, H. and J. Choi, "A Polarization Reconfigurable Textile Patch Antenna for Wearable IoT Applications", *International Symposium on Antennas and Propagation (ISAP)*, pp. 1–2, 2017.

32. Qin, P., A. R. Weily, Y. J. Guo and C. Liang, "Polarization Reconfigurable U-Slot Patch Antenna", *IEEE Transactions on Antennas and Propagation*, Vol. 58, No. 10, pp. 3383–3388, 2010.

33. Li, Y., Z. Zhang, W. Chen, Z. Feng and M. F. Iskander, "A Dual-Polarization Slot Antenna Using a Compact CPW Feeding Structure", *IEEE Antennas and Wireless*

Propagation Letters, Vol. 9, pp. 191–194, 2010.

34. Li, Y., Z. Zhang, W. Chen and Z. Feng, "Polarization Reconfigurable Slot Antenna with a Novel Compact CPW-to-Slotline Transition for WLAN Application", *IEEE Antennas and Wireless Propagation Letters*, Vol. 9, pp. 252–255, 2010.

35. Lee, S. W. and Y. J. Sung, "Simple Polarization-Reconfigurable Antenna with T-Shaped Feed", *IEEE Antennas and Wireless Propagation Letters*, Vol. 15, pp. 114–117, 2016.

36. Haupt, R. L. and M. Lanagan, "Reconfigurable Antennas", *IEEE Antennas and Propagation Magazine*, Vol. 55, No. 1, pp. 49–61, 2013.

37. Haridas, N., A. T. Erdogan, T. Arslan, A. J. Walton, S. Smith, T. Stevenson, C. Dunare, A. Gundlach, J. Terry, P. Argyrakis, K. Tierney, A. Ross and T. O'Hara, "Reconfigurable MEMS Antennas", *NASA/ESA Conference on Adaptive Hardware and Systems*, pp. 147–154, 2008.

38. Ha, S. and C. W. Jung, "Reconfigurable Beam Steering Using a Microstrip Patch Antenna with a U-Slot for Wearable Fabric Applications", *IEEE Antennas and Wireless Propagation Letters*, Vol. 10, pp. 1228–1231, 2011.

39. Li, Y., Z. Zhang, J. Zheng, Z. Feng and M. F. Iskander, "Experimental Analysis of a Wideband Pattern Diversity Antenna with Compact Reconfigurable CPW-to-Slotline Transition Feed", *IEEE Transactions on Antennas and Propagation*, Vol. 59, No. 11, pp. 4222–4228, 2011.

40. Masood, R., C. Person and R. Sauleau, "A Dual-Mode, Dual-Port Pattern Diversity Antenna for 2.45-GHz WBAN", *IEEE Antennas and Wireless Propagation Letters*, Vol. 16, pp. 1064–1067, 2017.

41. Chang, C., W. Lin, Y. Lin and W. Liao, "Diversity Antenna Design for Compact Devices of IoT Uses", *IEEE International Workshop on Electromagnetics: Appli-*

cations and Student Innovation Competition (iWEM), pp. 1–3, 2016.

42. Narbudowicz, A., M. J. Ammann and D. Heberling, "Switchless Reconfigurable Antenna with 360° Steering", *IEEE Antennas and Wireless Propagation Letters*, Vol. 15, pp. 1689–1692, 2016.

43. Qin, P., Y. J. Guo, A. R. Weily and C. Liang, "A Pattern Reconfigurable U-Slot Antenna and Its Applications in MIMO Systems", *IEEE Transactions on Antennas and Propagation*, Vol. 60, No. 2, pp. 516–528, 2012.

44. Tong, X., C. Liu, X. Liu, H. Guo and X. Yang, "Switchable ON-/OFF-Body Antenna for 2.45 GHz WBAN Applications", *IEEE Transactions on Antennas and Propagation*, Vol. 66, No. 2, pp. 967–971, 2018.

45. Chen, S., J. Row and K. Wong, "Reconfigurable Square-Ring Patch Antenna with Pattern Diversity", *IEEE Transactions on Antennas and Propagation*, Vol. 55, No. 2, pp. 472–475, 2007.

46. Raman, S., B. Graham, S. M. Crossan, N. Timmons, J. Morrison, V. A. Shameena and M. Pezholil, "Microstrip Fed Ground Modified Compact Antenna with Reconfigurable Radiation Pattern for BANs", *Loughborough Antennas Propagation Conference (LAPC)*, pp. 1–4, 2012.

47. da Conceição Andrade, A., I. P. Fonseca, S. F. Jilani and A. Alomainy, "Reconfigurable Textile-Based Ultra-Wideband Antenna for Wearable Applications", *10th European Conference on Antennas and Propagation (EuCAP)*, pp. 1–4, 2016.

48. Lim, I. and S. Lim, "Monopole-Like and Boresight Pattern Reconfigurable Antenna", *IEEE Transactions on Antennas and Propagation*, Vol. 61, No. 12, pp. 5854–5859, 2013.

49. Majid, H. A., M. K. A. Rahim, M. R. Hamid and M. F. Ismail, "Frequency and Pattern Reconfigurable Slot Antenna", *IEEE Transactions on Antennas and Prop-*

agation, Vol. 62, No. 10, pp. 5339–5343, 2014.

50. Akhavan, H. G. and D. Mirshekar-Syahkal, "Approximate Model for Microstrip Fed Slot Antennas", *Electronics Letters*, Vol. 30, No. 23, pp. 1902–1903, 1994.

51. ANSYS, *ANSYS High Frequency Structure Simulator (HFSS)*, `http://www.ansys.com/products/electronics/ansys-hfss`, accessed at August 2020.

52. Varteresian, J., *Fabricating Printed Circuit Boards*, Newnes, 2002.

53. Rogers, *Rogers Corperation RO3210 Laminate Datasheet*, 2019, `https://rogerscorp.com/-/media/project/rogerscorp/documents/advanced-connectivity-solutions/english/data-sheets/ro3200-data-sheet.pdf`, accessed at July 2020.

54. Dumanli, S., C. J. Railton, D. L. Paul and G. S. Hilton, "Closely Spaced Array of Cavity Backed Slot Antennas with Pin Curtains Walls", *IET Microwaves, Antennas Propagation*, Vol. 5, No. 1, pp. 38–47, 2011.

55. Long, S., "Experimental Study of the Impedance of Cavity-Backed Slot Antennas", *IEEE Transactions on Antennas and Propagation*, Vol. 23, No. 1, pp. 1–7, 1975.

56. Voltera, *Voltera V-One*, 2019, `https://www.voltera.io/`, accessed at July 2020.

57. Heinrich, W., "Quasi-TEM Description of MMIC Coplanar Lines Including Conductor-Loss Effects", *IEEE Transactions on Microwave Theory and Techniques*, Vol. 41, No. 1, pp. 45–52, 1993.

58. Ludwig, R. and P. Bretchko, *RF Circuit Design: Theory and Applications*, Prentice Hall, 2000.

59. NXP, *NXP Semiconductors BAP64-03 Silicon PIN Diode Datasheet*, 2019,

https://www.nxp.com/docs/en/data-sheet/BAP64-03.pdf, accessed at July 2020.

60. Mobashsher, A. T. and A. M. Abbosh, "Artificial Human Phantoms: Human Proxy in Testing Microwave Apparatuses That Have Electromagnetic Interaction with the Human Body", *IEEE Microwave Magazine*, Vol. 16, No. 6, pp. 42–62, 2015.

61. Garcia-Pardo, C., C. Andreu, A. Fornes-Leal, S. Castelló-Palacios, S. Perez-Simbor, M. Barbi, A. Vallés-Lluch and N. Cardona, "Ultrawideband Technology for Medical In-Body Sensor Networks: An Overview of the Human Body as a Propagation Medium, Phantoms, and Approaches for Propagation Analysis", *IEEE Antennas and Propagation Magazine*, Vol. 60, No. 3, pp. 19–33, 2018.

62. Pellegrini, A., A. Brizzi, L. Zhang, K. Ali, Y. Hao, X. Wu, C. C. Constantinou, Y. Nechayev, P. S. Hall, N. Chahat, M. Zhadobov and R. Sauleau, "Antennas and Propagation for Body-Centric Wireless Communications at Millimeter-Wave Frequencies: A Review [Wireless Corner]", *IEEE Antennas and Propagation Magazine*, Vol. 55, No. 4, pp. 262–287, 2013.

63. Moll, J., D. Wörtge, D. Byrne, M. Klemm and V. Krozer, "Experimental Phantom for Contrast Enhanced Microwave Breast Cancer Detection Based on 3D-Printing Technology", *10th European Conference on Antennas and Propagation (EuCAP)*, pp. 1–4, 2016.

64. Guraliuc, A. R., M. Zhadobov, O. De Sagazan and R. Sauleau, "Solid Phantom for Body-Centric Propagation Measurements at 60 GHz", *IEEE Transactions on Microwave Theory and Techniques*, Vol. 62, No. 6, pp. 1373–1380, 2014.

65. Mobashsher, A. T. and A. M. Abbosh, "Three-Dimensional Human Head Phantom with Realistic Electrical Properties and Anatomy", *IEEE Antennas and Wireless Propagation Letters*, Vol. 13, pp. 1401–1404, 2014.

66. Cil, E. and S. Dumanli, "Characterization of an Implanted Antenna inside a 3D Printed Multilayer Hip Phantom", *13th European Conference on Antennas and Propagation (EuCAP)*, pp. 1–4, 2019.

67. Ruvio, G., R. Solimene, A. Cuccaro, J. E. Browne, D. Gaetano and M. J. Ammann, "Experimental Microwave Breast Cancer Detection with Oil-on-Gelatin Phantom", *International Conference on Electromagnetics in Advanced Applications (ICEAA)*, pp. 871–874, 2013.

68. Joachimowicz, N., C. Conessa, T. Henriksson and B. Duchêne, "Breast Phantoms for Microwave Imaging", *IEEE Antennas and Wireless Propagation Letters*, Vol. 13, pp. 1333–1336, 2014.

69. Burfeindt, M. J., T. J. Colgan, R. O. Mays, J. D. Shea, N. Behdad, B. D. Van Veen and S. C. Hagness, "MRI-Derived 3-D-Printed Breast Phantom for Microwave Breast Imaging Validation", *IEEE Antennas and Wireless Propagation Letters*, Vol. 11, pp. 1610–1613, 2012.

70. Klemm, M., J. A. Leendertz, D. Gibbins, I. J. Craddock, A. Preece and R. Benjamin, "Microwave Radar-Based Breast Cancer Detection: Imaging in Inhomogeneous Breast Phantoms", *IEEE Antennas and Wireless Propagation Letters*, Vol. 8, pp. 1349–1352, 2009.

71. IT'IS, *IT'IS Foundation Dielectric Properties Database*, 2020, `https://itis.swiss/virtual-population/tissue-properties/database/dielectric-properties/`, accessed at February 2020.

72. Ghannouchi, F. M. and R. G. Bosisio, "Measurement of Microwave Permittivity Using a Six-Port Reflectometer with an Open-Ended Coaxial Line", *IEEE Transactions on Instrumentation and Measurement*, Vol. 38, No. 2, pp. 505–508, April 1989.

73. Alptekin, D., *Dual Band Microstrip Implantable Antenna Design for Biomedical Applications*, Ph.D. Thesis, Middle East Technical University, 2015.

74. Cil, E., S. Serbest, O. Baser, O. Tatar and S. Dumanli, *How to Make Your Own Probe (BOUNTENNA Research Laboratory Internal Report)*, Tech. rep., Bogazici University, 2019.

75. Gregory, A. and R. Clarke, "Tables of the Complex Permittivity of Dielectric Reference Liquids at Frequencies up to 5 GHz", *National Physical Laboratory Report*, 2012.